Geophysical Journal International

Geophys. J. Int. (2018) **215,** 825–843
Advance Access publication 2018 July 25
GJI Rock and Mineral Physics, Rheology

doi: 10.1093/gji/ggy305

KG^{2}B, a collaborative benchmarking exercise for estimating the permeability of the Grimsel granodiorite—Part 2: modelling, microstructures and complementary data

C. David,[1] J. Wassermann,[2] F. Amann,[3] J. Klaver,[4] C. Davy,[5] J. Sarout,[6] L. Esteban,[6] E.H. Rutter,[7] Q. Hu,[8] L. Louis,[9] P. Delage,[10] D.A. Lockner,[11] A.P.S. Selvadurai,[12] T. Vanorio,[13] A. Amann Hildenbrand,[4] P.G. Meredith,[14] J. Browning,[14] T.M. Mitchell,[14] C. Madonna,[15] J. Billiotte,[16] T. Reuschlé,[17] D. Lasseux,[18] J. Fortin,[19] R. Lenormand,[20] D. Loggia,[21] F. Nono,[21] G. Boitnott,[9] E. Jahns,[22] M. Fleury,[23] G. Berthe,[23] P. Braun,[10] D. Grégoire,[24] L. Perrier,[24] P. Polito,[25] Y. Jannot,[26] A. Sommier,[18] B. Krooss,[4] R. Fink[4] and A. Clark[13]

[1] *Université Cergy-Pontoise, Laboratoire GEC, Cergy-Pontoise, France. E-mail: christian.david@u-cergy.fr*
[2] *Université Cergy-Pontoise, Laboratoire* L2MGC*, Cergy-Pontoise, France*
[3] *RWTH Aachen, Aachen, Germany (formerly at ETH Zurich)*
[4] *EMR Group, Aachen University, Aachen, Germany*
[5] *Ecole Centrale de Lille, Lille, France*
[6] *CSIRO, Perth, Australia*
[7] *University of Manchester, Manchester, UK*
[8] *University of Texas, Arlington, TX, USA*
[9] *New England Research, White River Junction, USA*
[10] *Ecole des Ponts ParisTech, Champs sur Marne, France*
[11] *USGS, Menlo Park, USA*
[12] *McGill University, Montreal, Canada*
[13] *Stanford University, Stanford, USA*
[14] *University College London Earth Sciences, London, UK*
[15] *ETH Zurich, Zurich, Switzerland*
[16] *MINES ParisTech, PSL University, Paris, France*
[17] *IPGS,* UMR7516 *CNRS-Université de Strasbourg, Strasbourg, France*
[18] I2M *TREFLE, Bordeaux, France*
[19] *ENS, Laboratoire de Géologie, Paris, France*
[20] *Cydarex, Rueil-Malmaison, France*
[21] *Université de Montpellier, Montpellier, France*
[22] *Gesteinslabor, Heiligenstadt, Germany*
[23] *Institut Français du Pétrole énergies nouvelles, Rueil-Malmaison, France*
[24] *Université de Pau et des Pays de l'Adour, Pau, France*
[25] *The University of Texas at Austin, Austin, TX, USA*
[26] *LEMTA, Nancy, France*

Accepted 2018 July 24. Received 2018 July 20; in original form 2018 April 25

SUMMARY

Measuring and modelling the permeability of tight rocks remains a challenging task. In addition to the traditional sources of errors that affect more permeable formations (e.g. sample selection, non-representative specimens, disturbance introduced during sample acquisition and preparation), tight rocks can be particularly prone to solid–fluid interactions and thus more sensitive to the methods, procedures and techniques used to measure permeability. To address this problem, it is desirable to collect, for a single material, measurements obtained by different methods and pore fluids. For that purpose, a benchmarking exercise involving 24 laboratories was organized for measuring and modelling the permeability of a single low-permeability material, the Grimsel granodiorite. The objectives of the benchmark were: (i) to compare the results for a given method, (ii) to compare the results between different methods, (iii) to analyse the accuracy of each method, (iv) to study the influence of experimental conditions (especially

the nature of pore fluid), (v) to discuss the relevance of indirect methods and models and finally (vi) to suggest good practice for low-permeability measurements. To complement the data set of permeability measurements presented in a companion paper, we focus here on (i) quantitative analysis of microstructures and pore size distribution, (ii) permeability modelling and (iii) complementary measurements of permeability anisotropy and poroelastic parameters. Broad ion beam—scanning electron microscopy, micro-computerized tomography, mercury injection capillary pressure (MICP) and nuclear magnetic resonance (NMR) methods were used to characterize the microstructures and provided the input parameters for permeability modelling. Several models were used: (i) basic statistical models, (ii) 3-D pore network and effective medium models, (iii) percolation model using MICP data and (iv) free-fluid model using NMR data. The models were generally successful in predicting the actual range of measured permeability. Statistical models overestimate the permeability because they do not adequately account for the heterogeneity of the crack network. Pore network and effective medium models provide additional constraints on crack parameters such as aspect ratio, aperture, density and connectivity. MICP and advanced microscopy techniques are very useful tools providing important input data for permeability estimation. Permeability measured—orthogonal to foliation is lower that—parallel to foliation. Combining the experimental and modelling results provide a unique and rich data set.

Key words: Microstructure; Hydrogeophysics; Permeability and porosity.

1 INTRODUCTION

Following a workshop on 'The challenge of studying low-permeability materials' that was held at Cergy–Pontoise University in December 2014, a benchmark exercise in which several laboratories estimate the permeability of a single material was proposed to the attendees. The selected material was the Grimsel granodiorite (Switzerland) and the benchmark was named the 'KG^2B' project, from 'K for Grimsel Granodiorite Benchmark' (David *et al.* 2017). Multiple objectives were defined: (i) to compare the results for a given method, (ii) to compare the results between different methods, (iii) to analyse the accuracy of each method, (iv) to study the influence of experimental conditions (especially the nature of pore fluid), (v) to discuss the relevance of indirect methods and models and finally (vi) to suggest good practice for low-permeability measurements. The permeability measurements are presented in the companion paper. Here, we will focus on item (v) and present the results of microstructure analyses and permeability modelling.

Fluid flow processes in rocks are controlled by the geometrical properties of pore and/or cracks and the topology of the pore/crack network. Linking permeability to microstructural properties has always been a challenge in rock physics. A first step is to acquire high-quality data that allow thorough characterization of the pore space, preferably in 3-D. As we are dealing with a crystalline rock, the focus is on cracks rather than pores. Cracks in rocks can be approximated as planar features with small width or aperture, randomly oriented or not in a 3-D medium. Due to their limited resolution, optical microscopy techniques are not well suited for the study of cracks. SEM (scanning electron microscopy) studies have been commonly used to analyse cracks on thin sections at high magnification. Ion beam milling is recommended to avoid biased interpretation of the microcrack morphology and statistics (Wong, 1982). Crack statistics provided by SEM studies can be from 2-D analyses, from which 3-D parameters (like crack surface per unit volume) can be inferred using stereology (Fredrich & Wong, 1986). Recent advances in ion polishing now allow improved images of pore structures and crack networks to be obtained using BIB-SEM (broad ion beam—scanning electron microscopy, Klaver *et al.* 2015), or even 3-D structures from FIB-SEM (focused image beam) image stacks (Holzer *et al.* 2004). Wood's metal (WM) injection into the pore space greatly enhance pore and crack detection and analysis on SEM images (Hu *et al.* 2012; Klaver *et al.* 2015). High-resolution micro-CT (computerized tomography) techniques have become widely used to investigate the 3-D distribution of minerals and pores (Baker *et al.* 2012; Godel, 2013). With improvement of technology and analytical tools, submicrometre resolution can now be achieved with micro-CT imaging methods, but sometimes even this is insufficient to identify tiny cracks in crystalline rocks. One major advantage of micro-CT is that the technique is non-destructive and can be applied on centimetre-scale plugs. Pore or crack size distributions can be obtained by image analysis on SEM images (2-D analysis) or micro-CT reconstructed volumes (3-D analysis), and also by conducting mercury injection capillary pressure (MICP) tests on small plugs. MICP is commonly used in petrophysical studies to obtain the throat size distribution and capillary breakthrough pressure by injecting mercury under increasing pressure (Hu *et al.* 2015). The throat size distribution given by MICP does not actually match the pore size distribution (PSD) of the rock because of constrictions and ink-bottle effects in the pore space (Abell *et al.* 1999) but provides a first-order approximation that can be used in models. Other methods that provide insight into the PSD include the gas adsorption (or BET) method (Schull, 1948) and NMR (nuclear magnetic resonance) techniques (Josh *et al.* 2012).

Permeability models using microstructural data as input parameters have evolved since the pioneering work of Kozeny in the 1920s (Kozeny, 1927). A main challenge of all permeability models is to identify the characteristic length scale controlling permeability. This general statement rises from the permeability having the unit of squared length, but other factors like pore size variability and connectivity are also very important. Many different approaches have been proposed (Gueguen & Palciauskas, 1994). Originally based on the Kozeny–Carman equation (Kozeny, 1927), the equivalent channel model states that the characteristic length scale is the hydraulic radius, defined as the ratio between the pore volume and the pore surface area (Paterson, 1983; Walsh & Brace, 1984). In the equivalent channel model, permeability depends on bulk properties related to

the pore space (volume to surface ratio, porosity, tortuosity—an ill-defined parameter related to the increased path length in a 'tortuous' pore space) that, with the exception of tortuosity, are measurable at the sample scale. Statistical and effective medium models take advantage of the statistics of pore or crack geometries (Benson *et al.* 2006). For example, Gueguen & Dienes (1989) proposed a statistical model for crystalline rocks in which permeability depends on the mean crack aperture and radius, with cracks modelled as penny-shaped objects, on the average distance between cracks and on the fraction of connected cracks (which can be estimated from percolation theory). Only ensemble averages are estimated with limited input of the crack network topology. In contrast, network topology is taken into account in percolation and network models. For the percolation model proposed by Katz & Thompson (1986), the characteristic length scale is the so-called critical conductance (linked to a critical crack size), defined as the smallest conductance in the sample-spanning subnetwork made of conductances larger than the critical conductance. The critical length scale can be obtained from the breakthrough pressure in MICP experiments using Washburn's equation (Hu *et al.* 2015). Percolation models are supposed to work best when the PSD is very wide. In heterogeneous porous media, preferential flow paths (with similar properties as the critical percolation subnetwork) are more likely to occur (David, 1993).

Pore network modelling has been widely used for permeability prediction (Bernabé *et al.* 2003; Bauer *et al.* 2012). In such models fluid flows in pipes or cracks forming the bonds of a 3-D (or 2-D) lattice with fixed topology (e.g. a cubic lattice). The geometrical properties of the conducting elements follow the pore/crack size statistics obtained by SEM analysis or MICP *(*David *et al.* 1990). The flow equations are solved at each node and permeability is directly derived from Darcy's law, so does not depend on statistical averages (De Boever *et al.* 2012). Pore network modelling also allows the bond occupancy probability to be varied, so that networks with different average coordination number (or connectivity) can be considered for permeability estimation (David, 1993). Several of the permeability models mentioned above were tested by Casteleyn *et al.* (2011) on series of oolitic limestones from the Paris basin. Since the PSD of these rocks was not very heterogeneous, hence statistical and network models were successful in matching the measured permeability, while the percolation model underestimated the permeability by about one order of magnitude.

One of the objectives of the KG^2B benchmark was to conduct permeability modelling. Several models were selected by the participants. To achieve successful modelling, as discussed above, information is required about the rock microstructure (such as porosity, pore/crack aperture and length distribution and connectivity). We will present the results of a thorough microstructural analysis and from NMR and MICP tests, as well complementary data on anisotropy and poroelastic parameters measured on a voluntary basis by some participants.

2 THE KG^2B PROJECT: SUMMARY

In total, 30 laboratories from eight different countries volunteered to participate in KG^2B, and we received results from 24 laboratories that form the 'KG^2B Team'. The complete list of participants who sent results is given in Appendix A. A dedicated website https://labo.u-cergy.fr/∼kggb/ was created with information on the benchmark, including a webpage where the progress of the project could be followed on the 'KG^2B wheel', which was updated as soon as results were received from any of the participants. It took one year to collect all of the results. In total we collected 45 permeability values, including 39 measured values and six results from modelling, on which this paper will focus. Statistical, network, percolation and effective medium models were used. We add a seventh modelling result in which a rock sample is treated as an RC (resistance + capacitor) low-pass filter during pore pressure oscillation tests.

The Grimsel granodiorite was obtained from the Swiss Grimsel test site, a 450 m deep Underground Research Laboratory (URL). The 950 m long and 3.5 m diameter tunnels were excavated in 1983 by a full face tunnel boring machine (TBM) in hard rocks, mainly granite and granodiorite, at an altitude of 1730 m in the Central Aar Massif in Switzerland. The TBM excavation method limited perturbation of the host rock, with a quite small excavation damage zone (EDZ) around the tunnel (Egger, 1989). Along the tunnel, major damage zones are located in metre-scale shear zones or widely spaced discontinuities caused by regional deformation. Two cores of Grimsel granodiorite, each about 1 m long and of diameter 85 mm, were provided by our Swiss colleagues in September 2015. These cores were retrieved at a distance of 4–6 m from the tunnel of the Grimsel test site, far away from the EDZ influence. The cores were cut into small blocks at lengths requested by each participant (between 2 and 10 cm). A grain shape foliation is visible on the cores at an angle of about 20°–30° with respect to the core axis. The foliation is related to compositional banding of alternating dark biotite layers and quartz-rich layers (Schild *et al.* 2001). Natural and induced cracks have been observed in past studies (e.g. Smith *et al.* 2001). In particular there is a natural interconnected network of cracks producing about 1 per cent porosity in the granitic matrix. Stress release due to drilling and sample preparation outside the URL seems to be responsible for larger microcrack apertures than those observed directly *in situ* (Schild *et al.* 2001). As some laboratories provided permeability measurements in directions other than that required of the participants (i.e. the core axis direction), we will also discuss the permeability anisotropy.

The detailed analysis of the permeability measurements is given in the companion paper. Let us recall the most important results. For the whole data set of 39 measurements, the average permeability was 1.47×10^{-18} m^2; however four outliners were identified and removed, leading to an average permeability of 1.11×10^{-18} m^2 and a standard deviation of 0.57×10^{-18} m^2. A striking result was the large difference between measurements using gas or liquid as the pore fluids: the permeability to gas was about twice as large as the permeability to liquid ($k_{gas} = 1.28 \times 10^{-18}$ m^2 and $k_{liquid} = 0.65 \times 10^{-18}$ m^2). The model predictions presented in this paper will be compared to those values.

We will use the same convention as in the companion paper for presenting the data set. Each lab was assigned a number in increasing order with respect to the distance between their sample and the tunnel. Lab#01 worked on the sample closest to the tunnel, and Lab#24 on the farthest sample.

3 MICROSTRUCTURE AND POROSITY ANALYSES

3.1 Quantitative microstructural analysis

Here, we describe efforts to determine the main fluid flow pathways at the centimetre scale, which is the relevant scale for the laboratory experiments. To this purpose, several direct imaging methods were

used: automated optical microscopy of thin-sections, and BIB-SEM of intact or WM impregnated samples.

3.1.1 Methods

Two adjacent blue dye impregnated thin-sections of standard size were prepared perpendicular and parallel to the core axis from the original core sample (Fig. 1). Thin sections were automatically scanned with the Virtual Petroscan (ViP, Schmatz *et al.* 2010) in plane polarized (PPL) and crossed-polarized light (XPL). Porosity was segmented from the PPL image map (approximately 20 000 × 12 000 pixels, pixel size of 1.4 μm i.e. 2.8 cm × 1.68 cm ≈ 4.7 cm^2) by unsupervised isocluster classification and regrouped into porosity and matrix based on visual inspection followed by a boundary cleaning operation (dilation), all in ArcGIS 10.

From the same core sample, one subsample was prepared by BIB polishing to investigate the microstructure by SEM. Details on this technique are given by Klaver *et al.* (2012). Four areas were mapped at high resolution (10 000–20 000 x magnification) for quantitative analyses of the pore space. Porosity was segmented by a seed-and-grow algorithm (Jiang *et al.* 2015) and manually corrected where needed. Pore spaces with circularity below 0.2 and an axial ratio above 3 were automatically classified as cracks (including grain boundary cracks). Average crack intensity (expressed in crack number m^{-1}) and average crack thickness were calculated based on each pixel row from every map.

Another subsample was injected at 500 MPa with WM, which is a non-wetting alloy with wetting properties similar to mercury and which solidifies at room temperature. This method resembles mercury intrusion porosimetry (Klaver *et al.* 2015). We expected insignificant damage to the pores due to the material strength.

3.1.2 Visible porosity and pore size distributions

Over 60 000 pores were segmented from the thin sections and the largest pores were approximately 0.3 mm in equivalent diameter (Fig.2). The thin sections show different visible porosities: 0.71 per cent and 1.55 per cent for the parallel and perpendicular sections, respectively. This difference most likely occurred because the thin sections are not wholly representative at the centimetre scale regarding porosity. Alternatively, this contrast may owe to highly anisotropic pore shapes with large pore diameters parallel to the section and small diameters perpendicular to the section.

From SEM, the weighted average porosity in segmented maps perpendicular to the core direction is 0.45 per cent with a porosity of 0.54 per cent, 0.16 per cent, 0.64 per cent and 0.39 per cent in maps A, B, C and D, respectively (Figs 3a–d). However, most of the pore space (average 0.36 per cent) is associated with cracks, indicated in red in the figure. In map D, no cracks were counted, and all pores are interpreted as isolated pores within a single phase consisting mainly of K, Si, Al (Fig. 3e) and interpreted as K-feldspar. Other pore space-mineral associations are: (1) cracks at grain boundaries and within biotite (Fe, K, Mg, Al and Si); (2) minor pores and cracks along albite/plagioclase (Na/Ca, Al and Si) grain boundaries; (3) pores and cracks at quartz (Si and O) grain boundaries and fluid inclusions; and (4) fluid inclusions in apatite (Ca and P).

The PSDs of the imaged thin sections show a clear increase in pore frequency with decreasing equivalent diameter to about 6 μm (Fig.4a). The PSDs of the BIB-SEM maps show a clear peak at 200–300 nm equivalent diameter and another apparent increase below 100 nm. These smaller segmentations are below 18 pixels in size. They are interpreted as noise and hence excluded from the analyses in Fig.4(b), which shows normalized frequencies (number of pores divided by the imaged area and bin width). Taking into account both pores and interpreted cracks, only maps B and C show comparable best fits. The fact that the normalized PSDs do not show uniform best fits indicates that pore space may have been underestimated due to the large grain sizes and other heterogeneities.

Considering only the interpreted cracks in red (Figs 3a–d), the average crack thickness is 283 nm, within the visible range in Fig. 4(a). The average crack intensity over maps A–C is 14 749 cracks m^{-1}.

3.1.3 Pore connectivity

The WM-filled cross-section is shown in Fig. 5; the minerals are mostly biotite, albite, plagioclase and quartz (Fig. 5a). Most of the WM is located in the cracks. Most of the WM-filled cracks seem to be associated with biotite (Fig. 5b), and have widths of approximately 0.2–1 μm (Fig. 5c).

3.1.4 Synthesis of microstructural analysis

Macroscopic investigation reveals minerals of several centimetres in size, indicating that microstructural investigations limited to two adjacent thin sections are most likely not representative of porosity at the centimetre scale. The variability in porosity at the thin-section scale is significant (with values of 0.71 per cent and 1.55 per cent). However, the expected order of magnitude of porosity (about 1 per cent) is attained. A greater number of realizations would be necessary to achieve representativeness in a statistical sense.

In addition ViP-BIB-SEM investigations provided PSDs, enabling comparison with bulk measurements, and revealed pore-mineral associations which can help with upscaling scenarios. Most of the pore space is visible with optical microscopy, indicating that the relevant pores for storage are in the submillimetre to micrometre range. However, the pore connections are most likely in the submicron range as indicated by the BIB-SEM investigations, which revealed significant cracks and grain-boundary features in that range. The WM-BIB-SEM investigations also indicate that crack flow is the most important transport process. The WM-filled cracks tend to be wider and are connected in 2-D, perhaps opened due to the high pressures (while closing smaller cracks). This hypothesis is the subject of ongoing research.

This analysis is complemented by simplified calculations of permeability in Section 4, which assume that biotite is the main contributor to fluid flow, and that at room conditions the rock has an average porosity of 0.45 per cent, a crack aperture of 283 nm and a crack density of 14 749 cracks m^{-1}. These estimates provide insights into the key factors controlling the transport properties and flow paths identified by microscopy.

3.2 Microstructure study using micro-CT

A microtomography study was conducted at CSIRO Perth on a small sample of Grimsel granodiorite with 4 mm diameter and 10 mm length. The micro-CT equipment is the XradiaTM Versa microtomography system (XVRM126). This system is composed of an X-Ray source, a rotating sample holder and an X-Ray detection system. The source is generated by the impact of a focused beam on a thin target; the spot size can vary from 1 to 5 μm depending

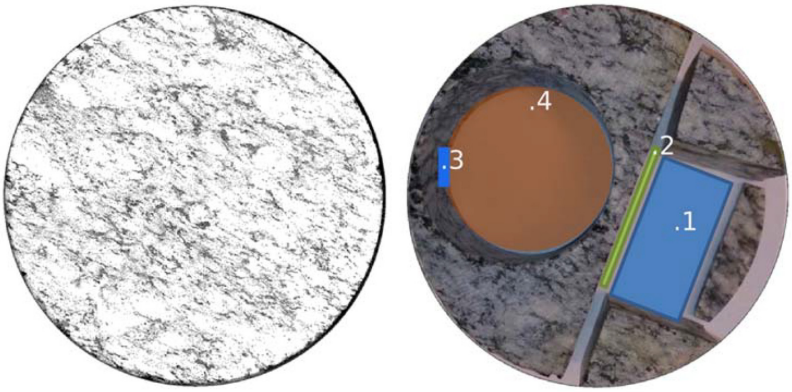

Figure 1. (1) Grimsel granodiorite core (left) and sampling (right) for thin sections perpendicular, and (2) parallel to the core axis, (3) for BIB-SEM and WM and (4) plug for permeability measurements for Lab#23.

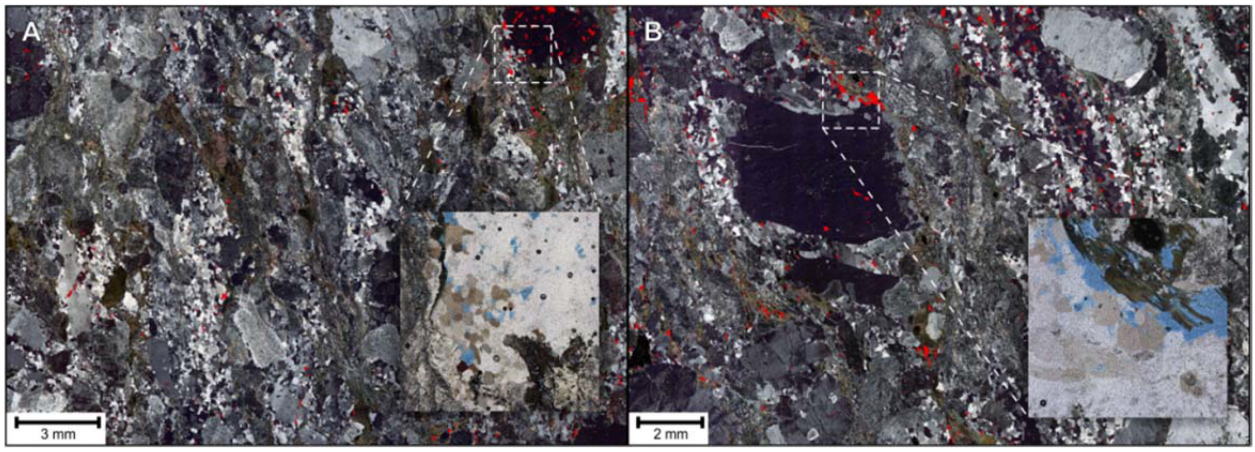

Figure 2. (a) ViP XPL maps overlain by pore segmentation in red of the parallel thin section and (b) perpendicular thin section. The insets show the blue dye filled pores in PPL.

on the operating conditions. The diverging geometry of the X-Ray results in a magnification of the object. The X-Ray source used allows application of voltage and power ranges from 40 to 160 kV and from 4 to 10 W, respectively. The X-Ray detector comprises several lenses mounted on a turret and the detector itself picking up X-Ray images of the sample. The mounted lens ranges from magnification level 0.4×–40× covering resolutions from few tens of micrometres to 0.7 μm in optimal conditions. The latter resolution can be obtained on 5 mm diameter samples. The images are generated by acquisition of a set of radiographs, while rotating the sample stepwise through a 360° rotation. For this study, the voxel size was 5 μm, enough to identify tiny pores (as shown also in BIB-SEM analysis) but insufficient to see the cracks, which have thicknesses dominantly in the submicrometre range. In Fig.6(a), four density maps with grey-scale coding are shown on cross-sections at different heights from top to bottom. The brighter areas correspond to denser minerals. Clearly, the rock appears very heterogeneous from the mineralogical viewpoint. The foliation oriented from left to right on the images is visible. Magenta circles highlight the presence of tiny, probably isolated pores, as discussed in the BIB-SEM section. 3-D reconstructions of the sample are shown in Fig.6(b). Again heterogeneity is ubiquitous. The reconstructions confirm that, at this scale, the investigated volume is below the REV (representative elementary volume, as discussed in the companion paper). The pore space reconstruction (excluding cracks) shows that the tiny pores are isolated and should not contribute significantly to macroscopic flow, unless connected through the crack network. Generally, the pores are uniformly distributed in the rock, although clusters are sometimes observed (Fig.6b). As mentioned in the BIB-SEM analysis, fluid flow is controlled by a 3-D network of cracks that is mostly located at grain boundaries or within biotite. Indeed such cracks not visible at the micro-CT scale were filled with WM (Fig.5) after WM injection.

3.3 Pore structure analysis with MICP and NMR

MICP can be used to measure pore structure characteristics such as total pore area, bulk density, porosity, pore throat distribution, permeability and tortuosity (Hu *et al.* 2015). Liquid mercury, which has a high surface energy and is non-wetting, is forced into the pore space under increasing capillary pressure. As mercury pressure increases, smaller pore throats are invaded. Mercury will only invade a pore throat when a sufficient mercury pressure, inversely proportional to the throat diameter is applied (Gao & Hu, 2013). This is expressed through the Washburn equation, which assumes a cylindrical pore shape (Washburn, 1921). For a 1 cm long cubic sample a typical MICP test takes 3–4 hr to complete, with measurable pore-throat size ranging from 3 nm to 36 μm for low-porosity (< 5 per cent) samples. Fig.7 shows the results obtained from MICP on the Grimsel granodiorite.

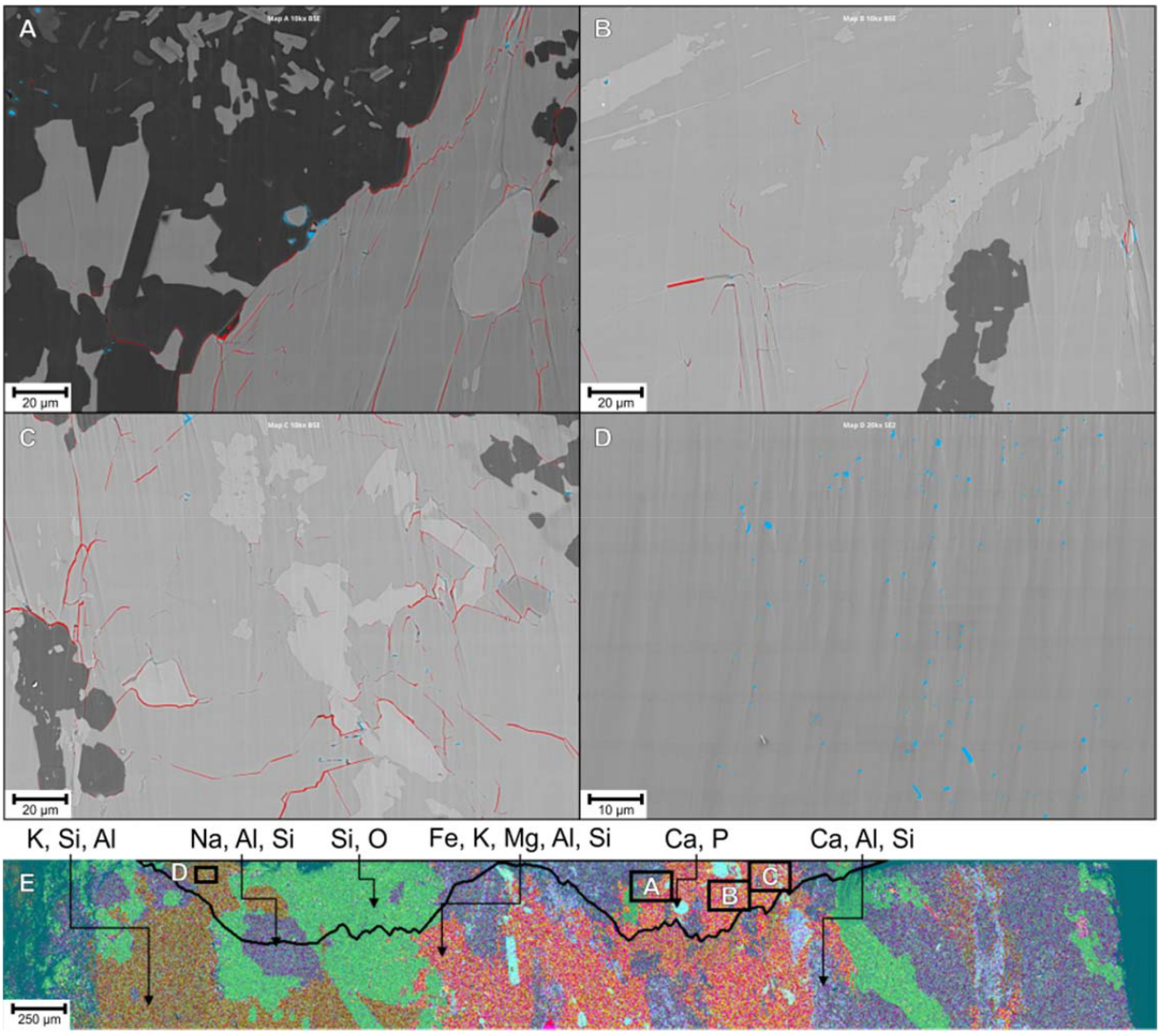

Figure 3. BSE (backscattered electron) image maps with pore space segmentation of maps a–d. Interpreted cracks are in red and pores in cyan. (e) The EDS (energy dispersive spectroscopy) overview map shows the locations of the maps with respect to BIB cross-sections and elemental compositions.

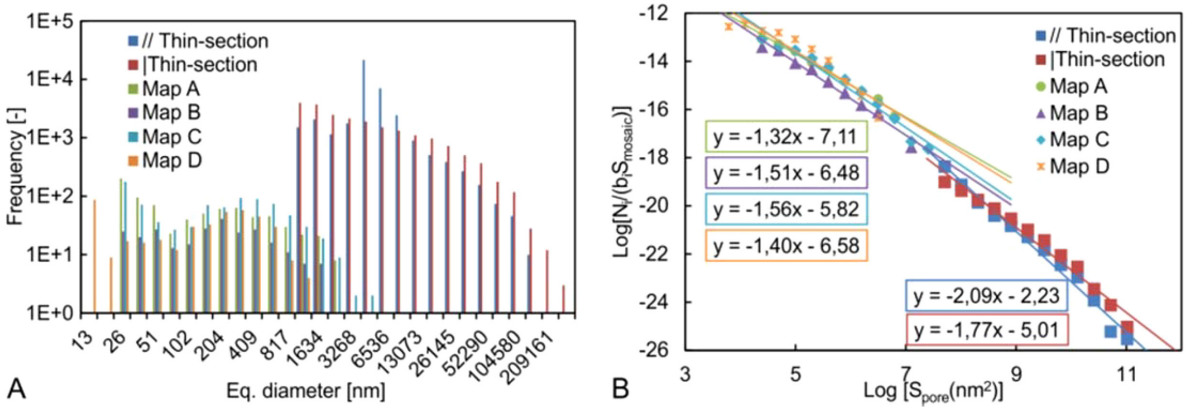

Figure 4. (a) PSDs of segmented porosity in the thin-sections and BIB-SEM maps. (b) Plot showing the PSDs, normalized over the imaged area for all segmented pores above 18 pixels in size, i.e. 6.5 µm, 144 and 72 nm for the thin sections, maps A–C and map D, respectively.

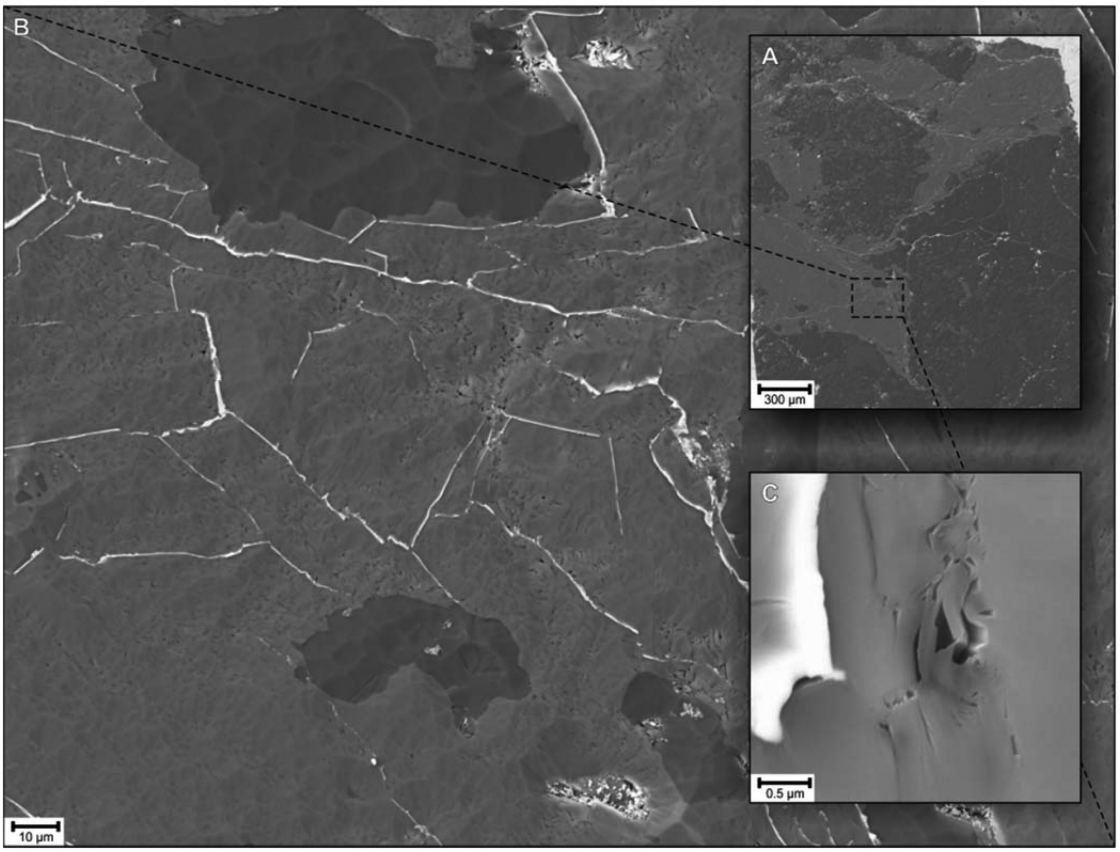

Figure 5. (a) Overview BSE (backscattered electron) image showing the WM intrusion (in white) at the sample scale. (b) Higher definition image map of the biotite dominated area shows connected crack networks in 2-D. (c) WM-filled crack 200 nm in width next to isolated pores.

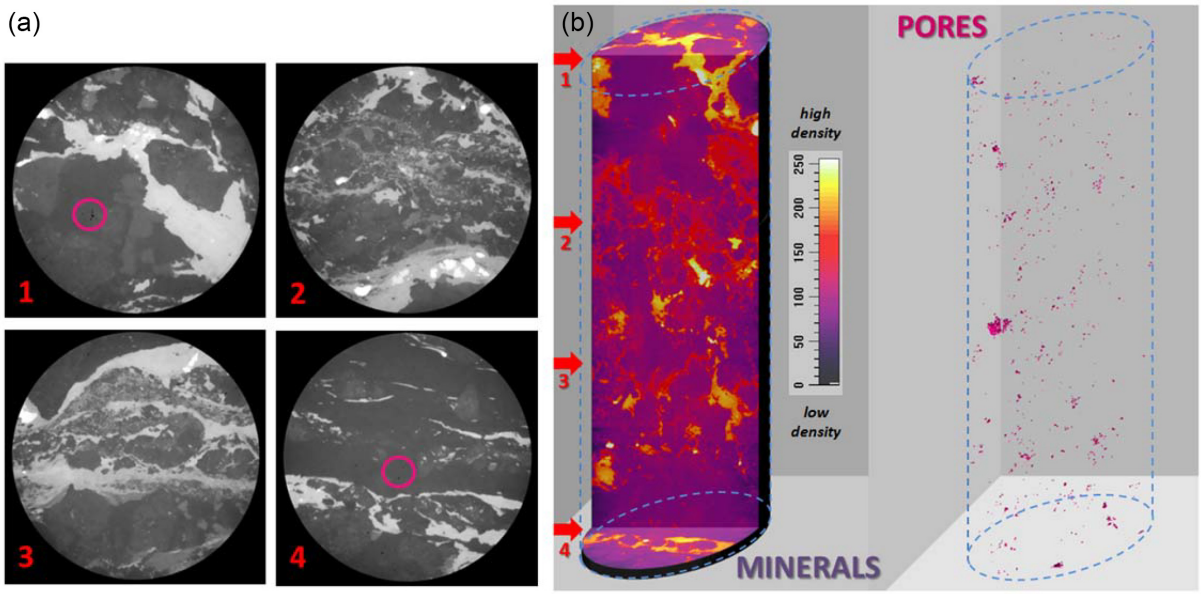

Figure 6. Micro-CT scan analysis of a small sample of Grimsel granodiorite (diameter 4 mm and length 10 mm). (a) Four sections at different heights from top to bottom; the pink circles highlight some pores (black spots). (b) Left, 3-D reconstruction of the matrix density map (8 bits colour coding), with red arrows indicating locations of the four cross-sections; right, 3-D map showing isolated or clustered tiny pores. The cracks evidenced by BIB-SEM analysis could not be resolved by this technique.

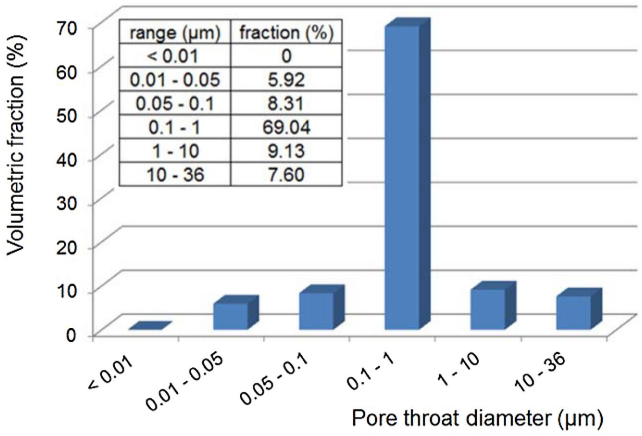

Figure 7. Throat size distribution derived from MICP on the Grimsel granodiorite.

The porosity provided by the mercury injection test at the highest capillary pressure is 0.59 per cent, lower but close to the average porosity found by other teams using different techniques (0.77 per cent). This is probably linked to the smaller size of the MICP plug compared to the permeability samples. A very strong peak is observed on the histogram, corresponding to a pore throat radius in the range between 0.1 and 1 μm.

In Fig. 8, we present the results of NMR spectroscopy conducted on five small plugs (diameter 25 mm and length 22 mm) saturated with water under vacuum and 13 MPa hydrostatic pressure, using a 2 MHz GeoSpec2 from Oxford-GIT Ltd Low-field proton NMR provides the transverse relaxation time T_2 from which bulk and bound water distributions can be extracted (Dillinger & Esteban, 2014). For the saturated state (Fig. 8a), the results are very consistent, with one strong peak at $T_2 = 0.15$ ms and two weakest ones in the range 10–100 ms. Short relaxation times usually correspond to bound water (e.g. capillary pore sizes and clay bound water) and long relaxation times correspond to free (or mobile) water; Fig. 8 shows that, in the Grimsel granodiorite, most of the water in the pore space is bound water at 13 MPa hydrostatic pressure.

For these five plugs the NMR porosity ranges from 1.75 to 2.2 per cent (average 2.03 per cent) which agrees with the range found with direct measurements (see te hnext section). The five samples were also desaturated by centrifuge to achieve an equivalent capillary pressure of $\sim$ 6.9 bars, and NMR measurements were repeated (Fig.8b). Such experiments allow one to evaluate the relative amount of mobile water and irreducible water. Note that sample Y1 has a different behaviour than the others.

3.3 Porosity measured on plugs

We collected 35 porosity values using different methods (helium pycnometry, triple weight method, mercury injection and NMR). As with permeability, no systematic trend was found when plotting porosity values as a function of the distance to the tunnel (Fig.9a). However, more consistent values seem to occur in the first 80 cm. The average porosity is 0.0077 (i.e. 0.77 per cent) with a standard deviation of 0.0036 (Fig.9b).

These values measured on macroscopic samples are in good agreement with those derived from thin section analyses reported in Section 3.

4 PERMEABILITY ESTIMATION FROM MODELS

About 13 per cent of the permeability estimates collected during the benchmarking exercise were obtained from model predictions. Several models have been used and can be classified as statistical, percolation, free-fluid, pore network (PNM) and effective medium models. In addition, we propose a model based on the analogy with an RC filter circuit to interpret the results from pore pressure oscillation experiments. The idea was not to find a winner among the different models, but to show that with the experimental data set and observations of the rock microstructure, it is possible to estimate the permeability of the Grimsel granodiorite with a rather good precision. In addition, the different models provide additional constraints on the crack network (coordination number, effective crack length and asperities) that increase our knowledge on the rock properties.

4.1 Permeability estimation from statistical models

Past research on natural or artificial geomaterials (Scherer *et al.* 2007; Song *et al.* 2015) has shown that the order of magnitude of fluid permeability may be assessed with simple statistical models. This requires a number of assumptions, the first being that the fluid does not interact with the solids.

The pore network in a crystalline rock can be approximated by a 3-D array of orthogonal flat cracks with constant length and aperture $2w$ (w is defined hereafter as the half-aperture). The pore space in the Grimsel granodiorite is considered with such model, in which the aperture is replaced by the average crack width obtained from the BIB-SEM analysis. The simplest model derived from Poiseuille's law for flow into straight parallel cracks gives:

$$k = \phi w^2/3 \tag{1}$$

In real materials, the pores are non-circular, intersecting and tortuous, so that the equation above is oversimplified (Scherer *et al.* 2007). The BIB-SEM results in Section 3 yielded an average porosity $\phi = 0.45$ per cent and average crack aperture $2\ w = 283$ nm or 1 μm. This provides a permeability prediction of 3×10^{-17} m^2 if the main pore width is 283 nm, and 3.7×10^{-16} m^2 if the main pore width is 1 μm. As shown earlier, the order of magnitude of measured permeability for the Grimsel granodiorite is 10^{-18} m^2. This suggests that the main pore size for transport is sub-micrometric, rather on the order of 283 nm, taking into account that the permeability measurements were done at 5 MPa effective pressure whereas the porosity measurements were done on unstressed rock.

Alternatively, permeability can be estimated by a fracture-based relationship for laminar flow (Zimmermann *et al.* 2005):

$$k = 2\lambda_L w^3/3 \tag{2}$$

where λ_L is the linear frequency of fractures or cracks. Taking $\lambda_L = 14\ 749$ m^{-1} and again $2\ w = 283$ nm results in a predicted permeability of 2.8×10^{-17} m^2. However, considering that most of the cracks relevant for flow are associated with biotite, and assuming a biotite content of 40 per cent, the predicted permeability based on crack density is 1.1×10^{-17} m^2 (i.e. 11×10^{-18} m^2), in agreement with the prediction of the previous model. This value is also larger than the average measured permeability by one order of magnitude, but again corresponds to the unstressed rock.

Although this analysis is quite simplistic, it provides useful insights into the location of fluid pathways and relates permeability measurement to microstructure quantification. Further analysis

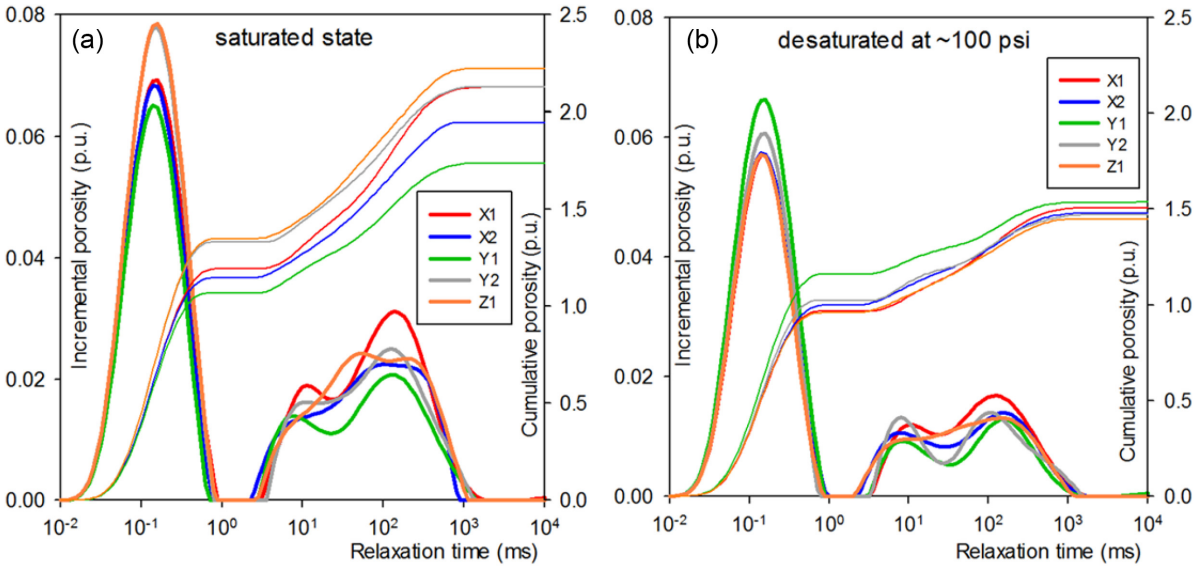

Figure 8. NMR transverse relaxation time T_2 spectra and associated cumulative porosity in five small core plugs of Grimsel granodiorite (a) under water saturated conditions, and (b) a desaturated state at ~ 6.9 bars.

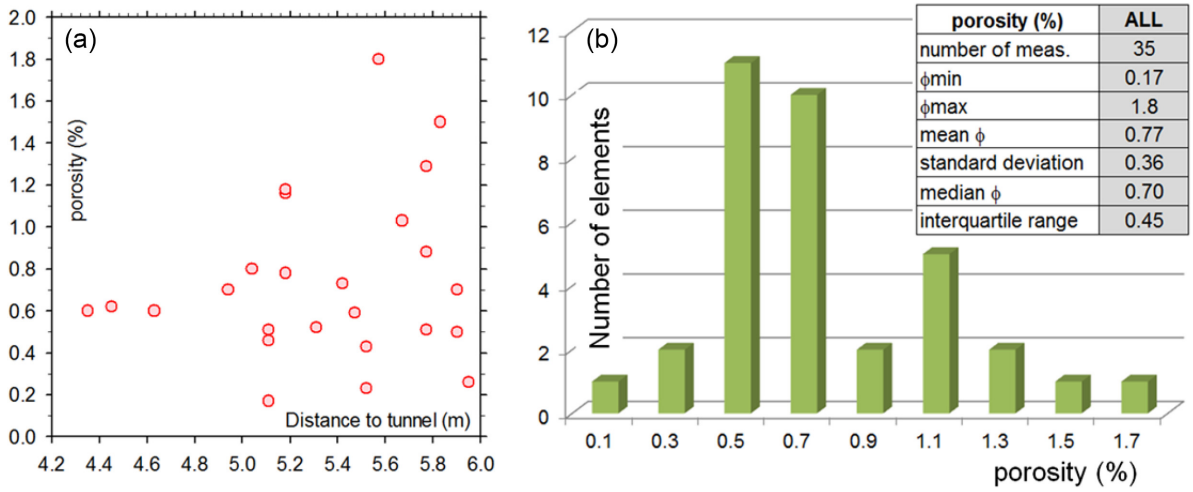

Figure 9. (a) Porosity vs distance to the tunnel. (b) Statistics of porosity measurements on plugs.

could be done by 3-D pore quantification and modelling, as done by Song *et al.* (2016) for a tight sandstone (with crack-like pores). Such analyses allow us to assess the contributions of different pore (crack) sizes to transport, material anisotropy and the effect of stress on permeability variations.

4.2 Permeability estimation from pore network modelling

Permeability simulations were conducted using a 3-D PNM described in Casteleyn *et al.* (2011). The input data required for such modelling include (i) an analytical description of the pore (or crack) size distribution, (ii) the average pore (or crack) shape and (iii) the rock porosity. In the Grimsel granodiorite, fluid flows through a network of cracks with low aspect ratio (Fig.5). In the PNM simulation, fluid flows through a network of pipes with elliptical cross-section. For sake of simplicity, all the pipes have the same aspect ratio ξ and constant length L_P (David, 1993). MICP provides an estimate of the crack aperture distribution (equivalent to the throat size diameter in Fig. 7) which corresponds to the minor axis 2 w of the elliptical pipes in the model; the semimajor axis R given by $R = w/\xi$ in the model corresponds to the half-width of the cracks. The local conductance of each bond is given by $\pi w^4/(4L_P\xi(1+\xi^2))$ (David, 1993). The experimental crack aperture distribution (Fig. 7) is modelled by a lognormal distribution in the range (0.01 μm, 30 μm) with a peak centred at 0.5 μm. The PNM is a cubic lattice with 20 nodes in each direction (Fig.10); the pipes are located at the branches of the lattice. An algorithm generates as many aperture values as pipes in the network (about 24 000), following the lognormal distribution. These aperture values are randomly assigned to the pipes in the network. The constant pipe length is derived from the 'network porosity' which must match the rock porosity. For sake of simplicity the network porosity was fixed at 1 per cent, close to the average porosity value measured on plugs. Fluid flow is simulated by imposing a constant pressure gradient across any pair of opposite faces of the network (David *et al.* 1990) and the permeability is derived from the net flow rate at the outlet face using Darcy's law. The whole process is repeated 10 times to obtain an average permeability and standard deviation. Several simulations were conducted for three different

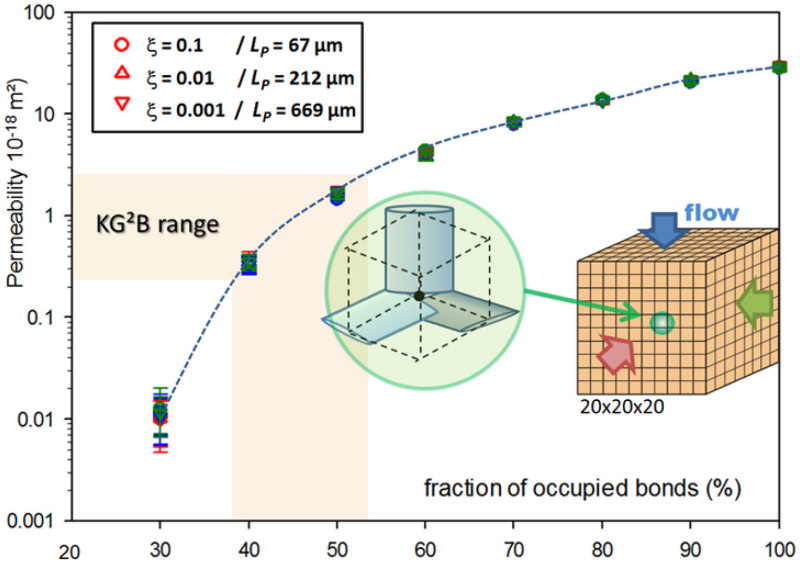

Figure 10. Results of permeability simulation using a 3-D pore network model on a 20 × 20 × 20 cubic lattice. Cracks are represented by pipes with elliptical cross-sections with minor axes derived from MICP data, constant aspect ratio and constant length. Three aspect ratios were considered: 0.1 (circles), 0.01 (upward triangles) and 0.001 (downward triangles). Colours red, blue and green define the directions in which permeability is calculated. Error bars correspond to the standard deviation of permeability values for 10 network realizations with the same statistical properties.

values of the aspect ratio in the range $\xi = 0.001$, 0.01 and 0.1 (Fig. 10). The simulations were done for different bond occupancy ratios until permeability fell to zero (the percolation threshold); this can be achieved by randomly removing pipes in the network until a selected value of bond occupancy is achieved.

The results of PNM simulations show that (i) permeability decreases when the fraction of pipes in the network decreases, with a sharp fall near the percolation threshold (0.25 for a cubic lattice), (ii) permeability is the same in all three directions within numerical errors and (iii) permeability is not changed by the pipe aspect ratio. This last result shows that permeability is essentially controlled by the crack aperture distribution which is the same in all simulations. For 100 per cent bond occupancy, the coordination number is equal to 6 and the network permeability is 28×10^{-18} m^2. Such a high coordination number (and permeability) is probably much too high for the Grimsel granodiorite.

The experimental permeability range found in the benchmarking exercise is highlighted in Fig. 10. This range is consistent with a fraction of occupied bonds between 38 per cent and 53 per cent, thus a mean coordination number probably lower than 3, a reasonable value for a hard rock in which crack connectivity is expected to be low. The crack network in Fig. 5 suggests an average coordination number close to 3, although it is hard to imagine what the real 3-D coordination number is from 2-D images. Given the crack lengths observed in Fig.5 (tens of micrometres) and the PNM results (Fig.10), our simulations suggest that the crack aspect ratio should range between 10^{-1} and 10^{-2}. As we tried to match the permeability measured at 5 MPa effective pressure, the inferred microstructural properties (aspect ratio and coordination number) correspond to that of the stressed rock. Note that the time-consuming numerical simulations were done at an early stage before the average porosity was determined from the measurements sent by the participants. The porosity value that was used (1 per cent) is far off the one obtained from observations at the microscale (0.45 per cent), but closer to the average sample porosity (0.77 per cent). In any case porosity has a minor influence on the permeability estimation in PNM, which is much more sensitive to the PSD.

4.3 Permeability estimation from effective medium modelling

Based on the microstructural data available, the Grimsel granodiorite is modelled as a homogeneous and isotropic solid, an aggregate of randomly oriented and naturally fused grains containing randomly oriented and spaced microcracks with finite diameter $2R$ and aperture $2\ w$. The number of microcracks per unit volume is N_V, and their aspect ratio is $\xi = w/R$. For sake of simplicity, the microcracks are modelled as oblate ellipsoids (thin cracks with $\xi << 1$). They can overlap/intersect so as to allow hydraulic connectivity and fluid flow through the rock at the macroscopic scale. The theoretical porosity of such a medium is given by Garboczi *et al.* (1995):

$$\phi = 1 - e^{V_C N_V} \tag{3}$$

where V_C is the volume of a single ellipsoidal micro-crack,

$$V_C = \frac{4}{3}\pi \xi R^3 \tag{4}$$

In this context, the crack density $\rho_V = N_V R^3$ is (Walsh, 1965; Sarout, 2012)

$$\rho_V = -\frac{3}{4\pi\xi}\log(1-\phi) \tag{5}$$

Let us assume that the network of microcracks in the Grimsel granodiorite is well above the hydraulic percolation threshold and that this network is the sole source of permeability (no background porosity). In this case, the permeability of the rock can be modelled using the concept of hydraulic radius (Gueguen & Dienes, 1989)

$$k \sim \alpha \phi m^2 \tag{6}$$

where $m = V_C/S_C$ is the hydraulic radius of ellipsoidal microcracks defined as their volume-to-surface ratio; and α is a dimensionless parameter derived from Poiseuille's law, related to the geometry of the hydraulically conducted network of microcracks, of the order of $\alpha \sim 1/3$ for a network of ellipsoidal microcracks (Sarout, 2012). The effective permeability of this cracked medium is explicitly related to

its microstructural parameters by (Sarout, 2012; Sarout *et al.* 2017)

$$k_{\text{eff}}\ (\phi, \xi, R) = \frac{16}{27}\ \frac{\phi R^2 \xi^2 \left(1-\xi^2\right)}{2\sqrt{1-\xi^2} + \xi^2 \log\left(\frac{2-\xi^2+2\sqrt{1-\xi^2}}{\xi^2}\right)} \tag{7}$$

This simple model explicitly relates the effective permeability of the microcracked rock to the crack porosity ϕ, the crack aspect ratio ξ and radius R or, equivalently, to the crack density ρ_V, ξ and R (Fig. 11). This is because ϕ and ρ are related through eq. (5) once the geometry of the cracks is set in the microstructural model (oblate ellipsoids with $\xi << 1$).

The experimental and microstructural parameters derived from measurements are the following:

(1) Measured average permeability @ $P_{\text{eff}} = 5$ MPa: 0.6×10^{-18} m^2 (liquid) to 1.3×10^{-18} m^2 (gas)
(2) Permeability extrapolated to $P_{\text{eff}} = 0$ MPa (room conditions): $k_{\text{exp}} = 1$–5×10^{-18} m^2
(3) Measured porosity @ $P_{\text{eff}} = 0$ MPa: $\phi_{\text{exp}} = 0.8$ per cent (cracks only)
(4) Porosity from microstructure @ $P_{\text{eff}} = 0$ MPa: $\phi_{\text{micro}} = 0.45$ per cent (cracks only)
(5) Crack half-aperture @ $P_{\text{eff}} = 0$ MPa: $w_{\text{micro}} = 140$ nm
(6) Linear crack number density @ $P_{\text{eff}} = 0$ MPa: $\lambda_{\text{L-micro}} = 14\ 749$ m^{-1}

One model parameter can be inferred from these data, the volumetric crack density ρ_V defined in eq. (5) which is related to the surface crack number density λ_A through the average of their squared crack radius $< R^2 >$ (Hadley, 1976)

$$\rho_V = \frac{3}{4\pi}\ \lambda_A \langle R^2 \rangle \tag{8}$$

The linear and surface crack number density are related through (Zimmermann *et al.* 2005)

$$\lambda_A = \frac{\pi}{2}\ \frac{\lambda_L}{\langle R \rangle} \tag{9}$$

Combining eqs (8), (9) and (5) yields

$$\begin{aligned} \rho_V &= \frac{3}{8}\ R\lambda_L \text{ and } \phi\ (\lambda_L, \xi, R) = 1 - e^{-\frac{1}{2}\pi R \xi \lambda_L} \\ &= \phi\ (\lambda_L, w) = 1 - e^{-\frac{1}{2}\pi w \lambda_L} \end{aligned} \tag{10}$$

so that the permeability in eq. (7) can be rewritten as

$$\begin{aligned} &k_{\text{eff}}\ (\lambda_L, \xi, w) \\ &= \frac{16}{27}\ \frac{w^2\left(1-\xi^2\right)}{2\sqrt{1-\xi^2} + \xi^2 \log\left(\frac{2-\xi^2+2\sqrt{1-\xi^2}}{\xi^2}\right)} \left(1 - e^{-\frac{1}{2}\pi w \lambda_L}\right) \end{aligned} \tag{11}$$

The data inversion strategy consists of the following steps:

(1) Using eq. (7), and the measured porosity ϕ_{exp} and permeability k_{exp}, we first define the effective crack radius function $R_{\text{sol}}(\xi)$ satisfying $k_{\text{eff}}(\phi_{\text{exp}}, \xi, R_{\text{sol}}(\xi)) = k_{\text{exp}}$,

$$\begin{aligned} &R_{\text{sol}}\ (\xi) \\ &= \frac{3}{4}\left[\frac{3k_{\text{exp}}}{\phi_{\text{exp}}\xi^2\left(1-\xi^2\right)}\left[2\sqrt{1-\xi^2} + \xi^2 \log\left(\frac{2-\xi^2+2\sqrt{1-\xi^2}}{\xi^2}\right)\right]^2\right]^{1/2} \end{aligned} \tag{12}$$

(2) Noting that by definition $R_{\text{def}}(\xi, w) = w/\xi$, we equate $R_{\text{sol}}(\xi) = R_{\text{def}}(\xi, w_{\text{sol}})$ and determine the effective crack half-aperture w_{sol} so that this equality is satisfied for all aspect ratios ξ.

(3) Using eq. (10), and noting that $\phi(\lambda_{\text{L-sol}}, w_{\text{sol}}) = \phi_{\text{exp}}$, we determine the linear crack number density $\lambda_{\text{L-sol}}$ satisfying this equality.
(4) Finally, using eq. (11), and setting $k_{\text{eff}}(\lambda_{\text{L-sol}}, w_{\text{sol}}/R_{\text{sol}}, w_{\text{sol}}) = k_{\text{exp}}$, we determine the effective crack radius R_{sol} satisfying this equality.
(5) Knowing w_{sol} and R_{sol}, we compute the effective aspect ratio of the cracks $\xi_{\text{sol}} = w_{\text{sol}}/R_{\text{sol}}$.

This strategy is implemented considering the permeability values estimated at room conditions in the range 1–5$\times$ 10^{-18} m^2 and a porosity of either $\phi = 0.8$ per cent (experimentally measured) or $\phi = 0.45$ per cent (determined from 2-D microstructure). Table 1 summarizes the results of the data inversion using these input parameters.

For the first two scenarios (run numbers 1 and 2) in Table 1 we observe that no value of the effective crack radius R can satisfy $\phi = 0.8$ per cent and $k = 10^{-18}$ m^2, or $\phi = 0.8$ per cent and $k = 5 \times 10^{-18}$ m^2. The derived aperture w and linear crack number density λ_{L} do not match the corresponding parameters estimated from 2-D microstructural analysis ($w_{\text{micro}} \sim 140$ nm and $\lambda_{\text{L-micro}} \sim 14\ 724$ m^{-1}).

The two other scenarios (run numbers 3 and 4) yield reasonable results, that is,

(1) An effective crack radius exists ($R = 0.92$–2.6 μm) that honours the measured permeability ($k = k_{\text{exp}} = 1 \times 10^{-18}$–$5 \times 10^{-18}$ m^2) and porosity ($\phi = \phi_{\text{micro}} = 0.45$ per cent)
(2) The inverted apertures ($w_{\text{sol}} = 39$–87nm) do not match the corresponding parameter estimated from 2-D microstructural analysis ($w_{\text{micro}} \sim 140$ nm and $\lambda_{\text{L-micro}} \sim 14\ 724$ m^{-1}). However, out of all scenarios, number 4 ($\phi = 0.45$ per cent and $k = 5 \times 10^{-18}$ m^2) offers the value of half-aperture ($w = 87$ nm) closest to that determined from 2-D microstructural analysis ($w = 140$ nm).
(3) The inverted crack number densities ($\lambda_{\text{L}} = 33\ 003$–$73\ 622$ m^{-1}) do not match the corresponding parameter estimated from 2-D microstructural analysis ($\lambda_{\text{L}} \sim 14\ 724$ m^{-1}). However, out of all scenarios, number 4 ($\phi = 0.45$ per cent and $k = 5 \times 10^{-18}$ m^2) offers the value of crack number density ($\lambda_{\text{L}} = 33\ 003$ m^{-1}) closest to the value determined from 2-D microstructural analysis ($\lambda_{\text{L}} = 14\ 724$ m^{-1}).
(4) The inverted crack aspect ratio ($\xi = 3.3$–4.2×10^{-2}) reflects a realistic crack geometry ($\xi << 1$).

In conclusion, scenario number 4 is the most realistic in view of the available experimental and microstructural data. To generate this scenario, we have used as an input $k = k_{\text{exp}} = 5 \times 10^{-18}$ m^2 and $\phi = \phi_{\text{micro}} = 0.45$ per cent. The model and data inversion strategy outputs are: an effective half-aperture $w \sim 90$ nm, an effective crack radius $R \sim 2.6$ μm, an effective aspect ratio $\xi \sim 3 \times 10^{-2}$ and a crack number density $\lambda_{\text{L}} \sim 33\ 003$ m^{-1} (or crack density $\rho_{\text{V}} \sim 0.025$).

Although the inverted w, R, ξ and λ_{L} are not exactly those determined from the microstructural analysis, they are reasonably close, and most importantly, they yield the expected porosity and permeability. The discrepancies can be explained as follows:

(1) The difference in crack aperture (90 nm versus 140 nm) could be due to (i) the resolution limits of the 2-D image; (ii) an undesired inflation of the cracks after WM injection; and/or (iii) the use of 2-D images to determine a 3-D parameter.
(2) The difference in crack number density (33 003 m^{-1} versus 14 724 m^{-1}) could be due to the heterogeneity of the rock and the fact that the images probe only a subvolume (in fact a 2-D surface) of the whole sample on which the porosity/permeability are measured.

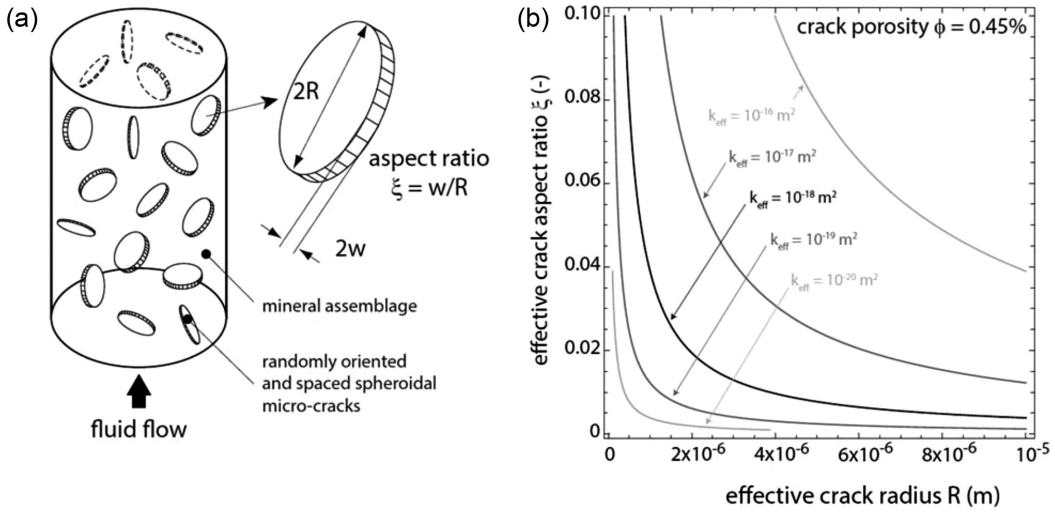

Figure 11. (a) Microstructural model of the Grimsel granodiorite. (b) Effective permeability predictions as a function of crack porosity, effective aspect ratio and crack radius.

Table 1. Results of the data inversion from effective medium modelling.

Run number	ϕ (per cent)	k (10^{-18} m^2)	w (nm)	λ_L (m^{-1})	R (μm)	ξ
1	0.8	1	29	99 009	None	None
2	0.8	5	65	44 173	None	None
3	0.45	1	39	73 622 ($\rho_V \sim 0.032$)	0.92	4.2×10^{-2}
4	**0.45**	**5**	**87**	**33 003 ($\rho_V \sim 0.025$)**	**2.6**	**3.3×10^{-2}**

(3) The difference between the measured porosity (0.8 per cent), and the porosity determined from 2-D microstructures (0.45 per cent) could be due to: (i) the heterogeneity of the rock and the fact that the images probe only a subvolume (in fact a 2-D surface) of the whole sample on which the porosity/permeability are measured, and/or (ii) a resolution limit of the porosity measurement as this type of crack porosity is inherently very small.

(4) The inverted crack radius $R \sim 2.6$ μm does not seem to qualitatively reflect the scale of the cracks highlighted by WM injection in Fig.5, where the cracks seem to be longer than 2.6 μm. However, the effective crack radius is determined from the effective hydraulic permeability of the rock which hosts natural and jagged cracks, perhaps with multiple contact points between asperities (see Sarout *et al.* 2017), so that the effective hydraulic radius is smaller than the cracks length visualized in the 2-D thin section. Other possible causes of discrepancy listed above could also contribute to the discrepancy in the inverted crack radius. For instance, the injection of WM could have inflated the crack network so that the cracks appear thicker (larger aperture), and longer (less contacts at asperities).

4.4 Permeability estimation from percolation model (MICP)

MICP results from the Grimsel granodiorite can be used with the Katz and Thompson equation (Katz & Thompson, 1986) as outlined in Hu *et al.* (2015). This model is based on percolation theory and states that a critical pore (or crack) size controls permeability. The critical pore size can be determined from the inflection point of the MICP cumulative intrusion curve when mercury starts to percolate into the pore space. According to this model, the permeability k is given by:

$$k = \frac{1}{89}(d_{\max})^2 \left(\frac{d_{\max}}{d_C}\right) \phi S(d_{\max}) \tag{13}$$

where $d_{\max}$ is the pore throat diameter at which conductance is maximum, d_C is the critical pore throat diameter at percolation threshold and $S(d_{\max})$ is the mercury saturation at a pressure corresponding to $d_{\max}$ (Hu *et al.* 2015). Using the throat size distribution given in Fig. 7 and the porosity derived from MICP on the same plug, a predicted permeability value of 1.05×10^{-18} m^2 for the unstressed rock is obtained, suggesting that MICP captures the correct characteristics of the fluid flow pathways at the sample scale.

4.5 Permeability estimation from free-fluid model (NMR)

NMR analysis is also able to predict the permeability from the T_2 relaxation time distribution (Josh *et al.* 2012) shown in Fig. 8. In this analysis, permeability prediction is based on the free fluid model by Coates *et al.* (1991). As the five samples were first measured saturated than desaturated after centrifuging, one can estimate the free fluid index (*FFI*, corresponding to the water removed at 6.9 bars equivalent capillary pressure) and the bound volume index (*BVI*, corresponding to irreducible water). Saturated and desaturated samples help to define the T_2 cut-off that separate *FFI* from *BVI* as shown in the example on sample X1 (Fig. 12a). The five samples record a T_2 cut-off around 30 ± 10 ms, very close to values found in the literature for quartz-rich rocks (around 33 ms).

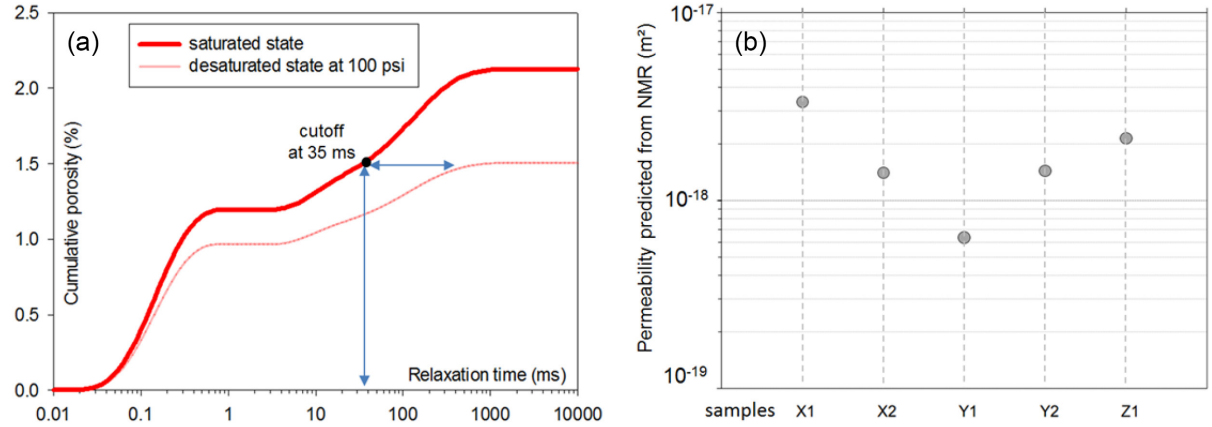

Figure 12. (a) Example of NMR cumulative porosity of sample X1 under saturated and desaturated conditions to measure the T_2 cut-off that separates mobile and irreducible water. (b) Predicted permeability from NMR in five small core plugs of Grimsel granodiorite using classical parameters from Coates.

As formulated in the Coates model (Coates *et al.* 1991), the NMR predicted permeability is given by:

$$k = \left(\frac{\phi}{\Gamma}\right)^4 \left(\frac{\mathrm{FFI}}{\mathrm{BVI}}\right)^2 \tag{14}$$

where Γ is a constant related to pore geometry. Using a standard value for Γ according to the Coates model ($\Gamma = 10$ when the permeability unit is mD (10^{-15} m^2) and porosity is in per cent, the five tested plugs have a predicted permeability ranging from 0.14 to 0.35 $\times$ 10^{-18} m^2 (average 0.20 $\times$ 10^{-18} m^2) except for sample Y1, which has a lower permeability (0.063 $\times$ 10^{-18} m^2) (Fig. 12b). These values are lower than the average permeability found in the benchmark (see the companion paper). However, they were obtained at 13 MPa confining pressure whereas the KG²B effective pressure target was 5 MPa. Taking into account the pressure dependence of permeability shown in the companion paper, the NMR predicted permeability values are in good agreement with the measured permeability range.

4.6 Permeability estimation from RC filter analogue

Here, we report a new way to analyse the data generated by pore fluid pressure oscillation experiments (see the companion paper) based on modelling the rock as an RC filter. The approach has been used by Mckernan *et al.* (2017) and Rutter and Mecklenburgh (2018). In contrast to the four previous models, this model is based on a physical analogue rather than microstructural data. Oscillatory flow of fluid through the pores of a rock is analogous to the flow of electricity through an RC network. A first-order RC filter is shown in Fig.13(a). This corresponds to a rock sample (the resistive element) of zero storativity (zero porosity), and the downstream reservoir corresponds to the capacitive element. The transfer function or gain $G = V_{\mathrm{out}}/V_{\mathrm{in}}$ depends on the frequency f because of the time required to charge the capacitor through the resistor. At low frequencies, the capacitor is infinitely resistant so a waveform applied as V_{in} passes unimpeded (provided the output does not draw current). Beyond the break frequency f_{B}, the capacitor can conduct so the R and C elements form the arms of a potential divider and the output is progressively attenuated as frequency is increased. This is a low-pass filter, because the unattenuated frequencies are low frequencies. The high-frequency waveform amplitude attenuation rate (gain) is always 20 dB per decade; it has a slope of -1 on a plot of log G versus log f. The linear prolongation of the high-frequency slope intersects the gain = 1 abscissa at a characteristic break frequency (or corner frequency) $f_{\mathrm{B}} = 1/(2\pi \mathrm{RC})$. The output (across the capacitor) of an RC filter also has a particular response to a step change in input voltage, with v_{out} decaying exponentially with time. This was the basis of the widely used pulse transient decay method proposed by Brace *et al.* (1968) for the measurement of permeability of tight rocks.

In addition to progressively attenuating the output waveform, the filter progressively shifts its phase over the frequency range between the two linear segments, from 0° to 90° (Fig. 13b). The gain G and phase shift θ can be expressed, respectively, as:

$$G = \frac{V_{\mathrm{out}}}{V_{\mathrm{in}}} = \frac{1}{\sqrt{1 + (f/f_B)^2}} \tag{15}$$

$$\theta = -\tan^{-1}\left(\frac{f}{f_B}\right) \tag{16}$$

Higher order low-pass filters can be formed by cascading first-order filters to simulate the behaviour of more porous rocks (higher storativity). A rock might be imagined as a series of such filters, with capacitive components corresponding to pore spaces connected by resistors that combine to form the total resistance to flow. Each RC element in series can apply an additional phase shift, but many such phase shifts will result in severe attenuation. Many possible topologies of R and C combinations can be imagined, with the final capacitor corresponding to the downstream volume of the permeameter. Analysis of such combinations is beyond the scope of this paper. Smaller ratios of rock storativity to downstream storage translate to smaller phase shifts for a given gain, so that the behaviour more closely resembles that of a first-order filter.

This approach was evaluated on a Grimsel granodiorite sample (called hereafter core C, cut at a high angle to the foliation), to investigate how similar its behaviour is to that of an RC filter. Pore fluid pressure oscillation tests were conducted with a pressure cycling period ranging from 50 to 12 800 s (i.e. 7.8 $\times$ 10^{-5} s^{-1} $< f <$ 2 $\times$ 10^{-2} s^{-1}). Fig. 14(a) shows a plot of log G versus log f for the driving waveform when total confining pressure is 20.0 MPa and pore pressure is 15.5 MPa. As expected the behaviour is similar to that of an RC filter with log $f_{\mathrm{B}} = -2.869$ (i.e. $f_{\mathrm{B}} = 1.35 \times 10^{-3}$ s^{-1}). The slope in the frequency-dependent region is -1.16, slightly greater than unity, as might be expected for the small degree of storativity (non-zero porosity) within the rock specimen.

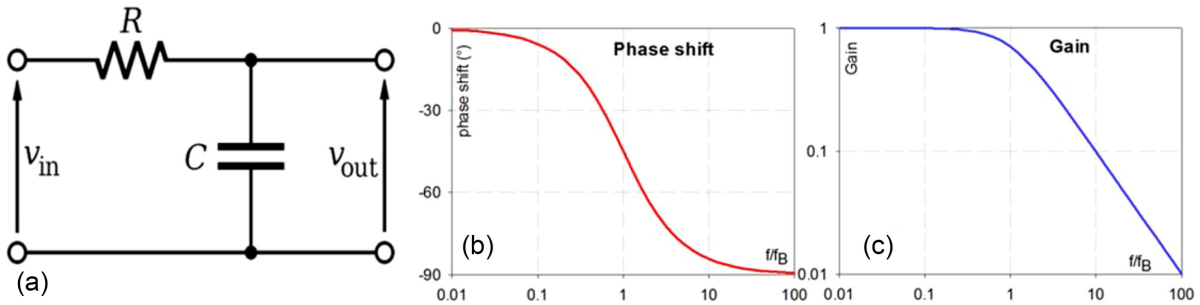

Figure 13. (a) A first-order electrical low pass filter analogous to fluid flow through a resistant rock R of zero storage capacity, with a capacitor C analogous to the downstream storage reservoir. Variation of (b) phase shift and (c) gain A with applied waveform frequency for a low-pass electrical filter.

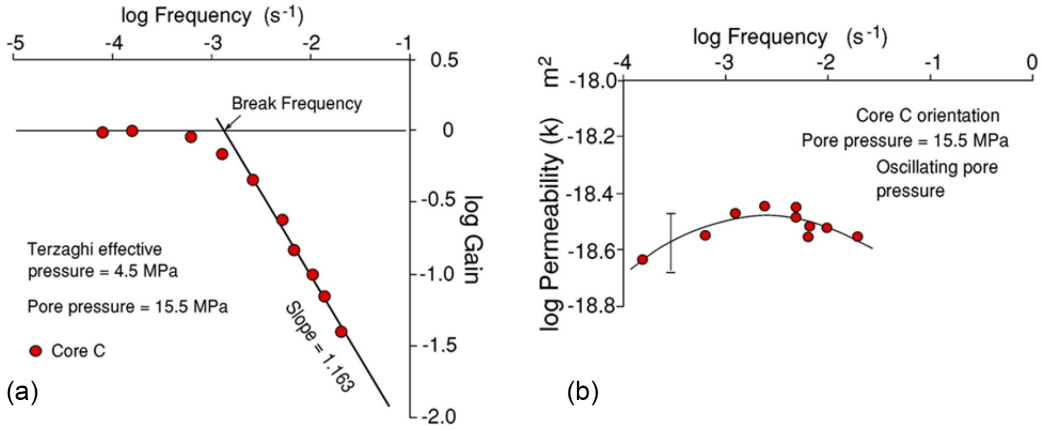

Figure 14. (a) Plot of log G versus log f for core C at 4.5 MPa effective pressure and 15.5 MPa pore pressure of argon gas. This is typical of rock behaviour as a first-order filter with very small storativity in the rock sample (slope of −1.16 close to unity). (b) Frequency dependence of permeability calculated for the individual data. The peak in the convex upward curve corresponds to the break frequency. The average of the log k data lying above the break frequency is −18.52.

The fluid flow analogues of resistance R and capacitance C are:

$$R = \frac{L\mu}{Ak} \text{ and } C = \beta_D \tag{17a}$$

where L and A are the length and cross-sectional area of the sample respectively, and β_D is the storage of the downstream reservoir (m^3 Pa^{-1}). Permeability can therefore be calculated from the break frequency provided that the frequency dependence of gain is measured at constant confining pressure and pore pressure conditions:

$$k = 2\pi\mu\,(L/A)\,\beta_D f_B \tag{17b}$$

This yields $k = 0.47 \times 10^{-18}$ m^2 for the tested sample. Leaving aside the most extreme values of very small or very large gain, the average of all the individual permeability measurements is $k = 0.30 \times 10^{-18}$ m^2. The plot of log k versus log f (Fig. 14b) shows slight upward convexity, similar to what was found for a sandstone by Song and Renner, (2007). One of the KG^{2}B labs (Lab#18, see the companion paper) measured a permeability of 0.501×10^{-18} m^2 on this sample with the standard approach for analysing pore pressure oscillation tests (Bernabé *et al.* 2006), and 0.582×10^{-18} m^2 using a transient pulse test.

5 COMPLEMENTARY OUTCOME OF THE BENCHMARKING EXERCISE

In this section, we present additional data produced by the KG^{2}B team in their study of the Grimsel granodiorite core samples. This data set is not as exhaustive as the permeability data set because it was done on a voluntary basis with no specific instructions.

5.1 Permeability–porosity relationship

A log–log plot of permeability versus porosity (Fig.15) shows a cloud of data points approximately consistent with the expected trend of permeability increase with increasing porosity. Two special points are highlighted: (i) point A was considered as an outlier in the statistical analysis of the permeability data set (see the companion paper) due to its lower permeability which can be explained by its porosity being much lower than all the others, and (ii) point B was also considered as an outlier due to its high permeability which cannot be explained by an anomalous porosity. The correlation is not very good, which is not really surprising as permeability is controlled by the geometrical properties (pore size and shape, topology and connectivity) of the 3-D pore or crack network and not simply by the bulk porosity. Nevertheless, a simple power law with an exponent equal to 2 (Fig.15) accounts reasonably well for the weak permeability–porosity correlation. A power-law relationship between permeability and porosity has often been invoked (e.g. David *et al.* 1994, and references therein). Wang *et al.* (2016) found an exponent between 4 and 5 in their permeability–porosity correlation for two granite gneiss samples. In our KG^{2}B experiments, porosity was measured at room conditions whereas permeability was measured at 5 MPa effective pressure. If both properties were

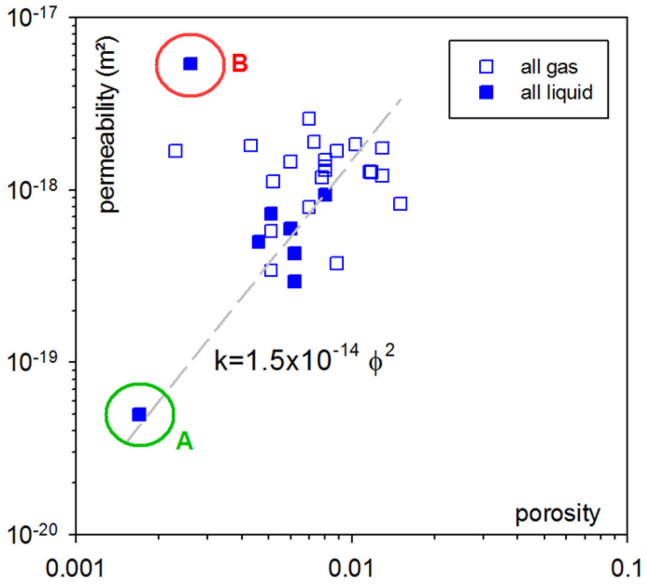

Figure 15. Correlation between permeability and porosity.

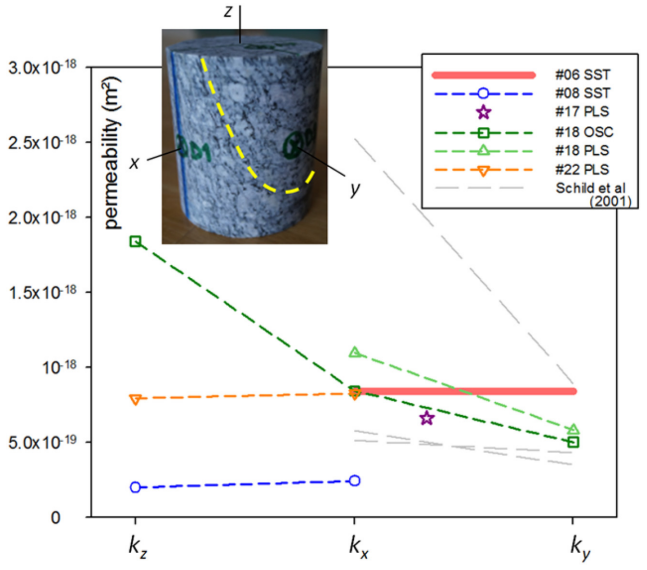

Figure 16. Permeability measured in direction *Oz,* along the core axis, *Ox* parallel to the foliation and *Oy* nearly perpendicular to the foliation. The grey lines are data published in Schild *et al.* (2001).

measured under the same pressure conditions, the correlation would probably have been better.

5.2 Permeability anisotropy

Three participants (Lab#8, Lab#18 and Lab#22) reported permeability measurements in more than one direction in order to test for permeability anisotropy. These data sets include the one presented in Section 4.6. which was obtained by Lab#18 using the oscillating pore pressure method and supplemented with measurements made in two other directions using the transient pulse method. The two other labs used the steady state and the transient pulse methods. All the anisotropy data were obtained using gas as the flowing fluid. The results are compiled in Fig.16, together with those from Schild *et al.* (2001). For the KG^2B core, an orientation nomenclature was adopted whereby *Oz* represents the direction parallel to the core axis, *Ox* is the direction perpendicular to *Oz* and parallel to the foliation; and *Oy* is perpendicular to both *Oz* and *Ox*. Note that *Oy* is nearly perpendicular to the foliation (∼70°). Schild *et al.* (2001) investigated permeability parallel and perpendicular to the foliation and for the sake of comparison those directions were associated with directions *Ox* and *Oy*, respectively. Overall, anisotropy emerges from the comparison between directions *Ox* and *Oy*, where the permeability along the foliation consistently measures higher than the one (quasi-) perpendicular to it (respective anisotropy coefficients of ∼50 per cent and ∼60 per cent for the OSC and PLS measurements of Lab #18). This result is qualitatively consistent with the data of Schild *et al.* (2001), albeit over a greater range of anisotropy coefficients. It also compares well with the velocity data of Schild *et al.* (2001) and the velocity measurements made during our screening of the KG^2B plugs [∼30 per cent *P*-wave anisotropy reported in David *et al.* (2017)].

When plugs in both *Ox* and *Oy* directions were tested, the permeability nearly perpendicular to foliation (along *Oy*) was systematically smaller than in the direction nearly parallel to foliation (along *Ox* or *Oz*). Little permeability anisotropy was expected to arise from the measurements made along *Oz* and *Ox*, as *Oz* is relatively close to the foliation. This is confirmed by the results of Lab#08 and Lab#22. The value obtained along *Oz* by Lab#18 is not consistent with that picture; it might be attributable to heterogeneity from sample to sample. More specifically, since permeability is considered as being largely controlled by microcracking in the biotite grain fraction, slight changes in biotite content and grain size from sample to sample could result in large baseline contrasts. A better assessment could be obtained if the same REV was measured along several directions as opposed to distinct plugs of various dimensions. Two additional participants (Lab#6 and Lab#17) measured the permeability only in radial directions: both values fall in the range of radial permeability found by the others. The sample tested by Lab#17 was oriented at about 30° from the foliation, and the radial permeability measured by Lab#06 is an average one (plotted with an horizontal line) derived from a radial water flow experiment on a hollow cylinder parallel to the core axis (Monfared *et al.* 2011) at 1.75 MPa effective confining pressure, lower than the KG2B target. Due to the limited number of samples, the anisotropy analysis is far from being as convincing as the general KG^2B data set.

5.3 Poroelastic parameters

In situ rock masses include pore, crack, fracture networks which are usually saturated or partially saturated with fluids, often with 2 or more fluid phases such as gas, water or oil. The degree of saturation, ranging between 0 and 1, is the ratio of volume of pore fluid in the pore space to the pore volume. Controlling saturation during laboratory tests is important for two main reasons: (i) to reproduce field conditions; and (ii) for intrinsic permeability estimates. For the latter purpose, full saturation of specimens with fluid used for measurement is essential (Zinszner & Pellerin, 2007). For measurements using gas, particular attention has to be paid to sample preparation and drying. For permeability measurement using liquids, key issues include expelling trapped gas and checking for full saturation with liquid phase. For measurement with water, flushing of de-aired water into the specimen, followed by a step-by-step back pressure increase, have been recommended in order to avoid additional gas entry and to force trapped gas into solution (Black and Lee, 1973). This method was successfully applied to a tight porous rock, the

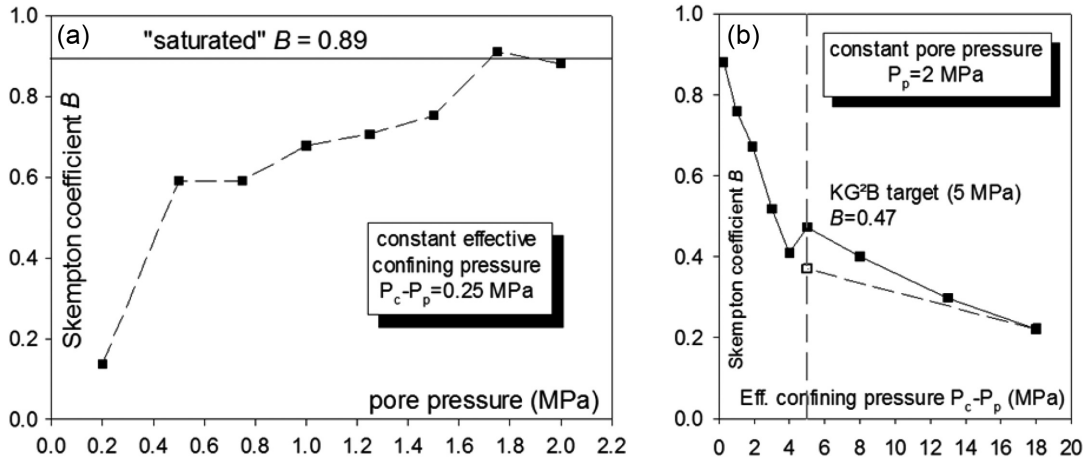

Figure 17. (a) Evolution of the Skempton's coefficient *B* versus pore pressure. (b) Evolution of the Skempton's coefficient *B* versus effective confining pressure at constant pore pressure (2 MPa).

Opalinus clay (Wild *et al.* 2015) and also in this study by Lab#04 on a Grimsel granodiorite sample. Between each back pressure step, the poroelastic response to hydrostatic confinement was checked in order to assess the degree of saturation. The isotropic Skempton's coefficient measurements, defined as $B = \Delta P_p/\Delta P_c$, the ratio of pore pressure change to confinement pressure change, should reach a plateau when all trapped gas bubbles are dissolved in the solution. For the Grimsel granodiorite initially filled with water under vacuum, a plateau is reached when the pore pressure exceeds about 1.8 MPa (Fig. 17a), and the 'saturated' Skempton's coefficient is $B = 0.89$ at 0.25 MPa effective confining pressure.

Once the 'saturation' pore pressure was reached, the confining pressure was increased at constant pore pressure ($P_p = 2$ MPa) to the KG^{2}B pressure target ($P_{\text{eff}} = 5$ MPa) and beyond. The increase of effective confining pressure resulted in a sharp drop of the Skempton's coefficient (Fig. 17b) to 0.47 at the target pressure, and even lower at higher pressures. This behaviour is probably linked to the progressive closure of cracks in the rock sample.

Another poroelastic parameter was determined by one of the participants (Lab#19), the Biot–Gassmann effective pressure coefficient α. This coefficient was obtained from several permeability measurements under different pressure conditions (both P_p and P_c). The effective pressure law $P_{\text{eff}} = P_c - \alpha P_p$ was established for permeability, and it was shown that the effective pressure coefficient α was equal to 1 (see the companion paper).

6 DISCUSSION

To complement the experimental permeability data set presented in the companion paper, we present additional data from microstructural analyses using BIB-SEM and micro-CT, as well as permeability predictions from various models. High-quality imaging with BIB-SEM technology allowed us to identify pores and cracks at the micrometre scale and their relation with the rock mineralogy. Most of the cracks are located within biotite or at grain boundaries. The WM injection technique, combined with SEM, provided detailed and realistic images of the actual crack network, its connectivity (from which an average coordination number can be estimated) and tortuosity. A statistical analysis provided relevant data on pore size, crack length and aperture, and porosity obtained from more than 60 000 elements; the amount and quality of these data provided valuable information for permeability modelling. Micro-CT imaging provided 3-D volume rendering of the matrix density as well as a 3-D map of pore locations. Two important conclusions could be drawn: (i) at the sample scale, the material appears to be very heterogeneous, with the size of heterogeneities exceeding the sample size and (ii) the pores resolved by micro-CT are isolated, confirming that fluid flow is controlled by a network of submicron cracks. It seems clear that the size of the samples studied (core sample with 4 mm diameter and 10 mm length) is well below the REV, which may explain the larger scatter in measured permeability values for small samples shown in the companion paper.

Table 2 summarizes the results of permeability modelling using microstructural data as input parameters. For each model, a short description is provided, and the input parameters are given.

(1) Both statistical models yield a permeability value of about 30×10^{-18} m^2, significantly larger than the mean outcome for the measured permeability data set ($\sim 1 \times 10^{-18}$ m^2). These models are based on an oversimplified representation of the pore space where heterogeneity is absent, so that analytical solutions for permeability can be calculated. The predicted values are likely higher because the microstructural data were obtained on stress-free samples, whereas permeability measurements were obtained at 5 MPa effective confining pressure. However, if one takes into account the pressure dependence of permeability shown in the companion paper, extrapolated permeability at zero effective pressure would give a value in the range $2–10 \times 10^{-18}$ m^2, still lower than the permeability predicted by both statistical models. This discrepancy suggests that the heterogeneous nature of the rock pore space is poorly accounted for in statistical models.

(2) In contrast, the percolation model proposed by Katz & Thompson (1986) takes advantage of the full mercury volume versus pressure curve obtained in MICP experiments. This model postulates the existence of a subnetwork spanning the rock sample, consisting of highly conducting cracks with conductance larger than a critical value. Heterogeneity is taken into account, the model prediction of the model ($\sim 1 \times 10^{-18}$ m^2) is in good agreement with the measured permeability despite the fact that the effective pressures do not match. MICP coupled with percolation modelling provides the correct length scale for permeability estimation.

(3) Generally consistent results were obtained for NMR-predicted permeability using the free fluid model. This model is based on NMR detection of the fraction of bound water in the pore

Table 2. Summary of permeability predictions obtained with six different models using input parameters based on microstructural data.

Model	Description	Input parameters	Permeability prediction
Statistical model	3-D array of orthogonal intersecting cracks with same length and aperture	Porosity, mean crack aperture	$k_{pred} = 30 \times 10^{-18}$ m^2
Statistical model (Zimmermann *et al.* 2005)	Array of parallel cracks with the same aperture	Linear density of cracks, mean crack aperture	$k_{pred} = 28 \times 10^{-18}$ m^2
Percolation model (Katz & Thompson, 1986)	Based on the estimation of the critical crack aperture at percolation threshold	MICP intrusion volume vs pressure graph, pore throat and saturation at threshold pressure, porosity	$k_{pred} = 1.1 \times 10^{-18}$ m^2
Free-fluid model (Coates *et al.* 1991)	Based on NMR relaxation time distribution	NMR T_2 spectrum, porosity, free and bound water fractions	0.13×10^{-18} m^2 $< k_{pred} < 0.33 \times 10^{-18}$ m^2 (@13 MPa)
Pore network model (David, 1993; Casteleyn *et al.* 2011)	3-D cubic network of pipes with elliptical cross-section and constant length	Crack aperture distribution from MICP, crack aspect ratio, porosity, fraction of occupied bonds χ	($\chi = 100$ per cent) $k_{pred} = 28 \times 10^{-18}$ m^2 ($\chi = 53$ per cent) $k_{pred} = 2.5 \times 10^{-18}$ m^2 ($\chi = 38$ per cent) $k_{pred} = 0.25 \times 10^{-18}$ m^2
Effective medium model (Sarout *et al.* 2017)	3-D random distribution of penny-shaped cracks	Crack density, porosity, crack aperture, crack aspect ratio	$k_{pred} = 5 \times 10^{-18}$ m^2

space. Although little information is captured regarding pore space geometry, the model was successful in predicting the correct range of permeability at the NMR operating confining pressure (13 MPa), based on the pressure dependence of permeability presented in the companion paper.

(4) The 3-D nature of fluid flow in porous rocks is accounted for in both the PNM and the effective medium model. The difference between these models is the topology of the crack network: cracks are located at bonds in a cubic lattice for the former, and randomly distributed for the latter. For both models, the number of input parameters is larger: porosity, crack aperture and aspect ratio, length of pipes in the PNM and crack density in the effective medium model. Not all of these parameters are well constrained either by MICP or microstructural data. Therefore, reasonable assumptions were made to find the best set of parameters to match permeability measurements at 5 MPa effective pressure. Interestingly, both models converge to a similar value of crack aspect ratio ($\sim 10^{-2}$), an apparently reasonable value based on the micrographs in Figs 3 and 5. Another outcome of the PNM is that a permeability prediction consistent with the measured value requires a coordination number close to three, again in agreement with the micrographs in Figs3 and 5. However, the models disagree regarding crack length, of order 100 μm for the PNM, and 1 μm for the effective medium model. Whereas the former value corresponds more or less to the actual crack length imaged in Fig. 5, the latter does not, and one may conclude that the effective medium model is unable to match all our observations. Nevertheless, as discussed in Section 4.3, the discrepancy may be explained by the presence of asperities and the jagged nature of observed cracks; in the effective medium model, an actual crack might be viewed as a combination of smaller cracks relevant for fluid flow.

7 CONCLUSION

In the companion paper, the complete data set of low-permeability measurements from a benchmarking exercise involving 24 laboratories was analysed; here we present complementary results focusing on (i) quantitative analysis of microstructures and PSDs, (ii) permeability modelling and (iii) measurements of permeability anisotropy and poroelastic parameters. BIB-SEM, micro-CT, MICP and NMR methods were used to characterize microstructures (both in 2-D and 3-D) and quantify PSD. WM injection was used to image the crack networks on 2-D images. All of these studies provided input parameters for permeability modelling using (i) basic statistical models, (ii) 3-D PNM and effective medium models, (iii) a percolation model using MICP data and (iv) a free-fluid model using NMR data. A new method for simpler analysis of pore pressure oscillation tests, modelling the rock as an RC electrical circuit, was also described for the case of small sample storativity. The models were generally successful in predicting the observed range of measured permeability using microstructural, MICP and/or NMR data. Whereas statistical models overestimate the permeability due to lack of information on heterogeneity, percolation, PNM and effective medium models are more relevant and provide additional constraints on crack parameters such as aspect ratio, aperture, density and connectivity. This confirms that MICP and advanced microscopy techniques are potentially able to provide useful input data for permeability estimation. Additional results to complement the measured permeability data set show that (i) the average porosity measured on plugs is 0.77 per cent ± 0.36 per cent, (ii) a weak power law with exponent 2 relates permeability to porosity, (iii) permeability measured—orthogonal to foliation is lower that—parallel to foliation and (iv) the Skempton's coefficient at 5 MPa effective pressure is about 0.5. A second round of benchmarking is currently under way, with another tight material, the Cobourg Limestone. Additional challenges are expected in this benchmark, project called KCL as the permeability is in the range of 10^{-21} m^2.

ACKNOWLEDGEMENTS

This project was partially funded by a grant from the 'Fondation de l'Université de Cergy-Pontoise'. We thank Belinda Godel for conducting the micro-CT study on a Grimsel granodiorite sample at CSIRO Perth. The KG²B project is supported by the GIS Géosciences Franciliennes (http://www.geosciences-franciliennes.fr) within the research group on 'Low Permeable Media'. We thank Yves Bernabé and Steve Ingebritsen for their thorough early review of both companion papers, Phil Benson and Jamie Farquharson for their constructive review of the submitted manuscript.

REFERENCES

Abell, A.B., Willis, K.L. & Lange, D.A., 1999. Mercury intrusion porosimetry and image analysis of cement-based materials, *J. Colloid Interface Sci.*, **211**(1), 39–44.

Baker, D.R., Mancini, L., Polacci, M., Higgins, M.D., Gualda, G.A.R., Hill, R.J. & Rivers, M.L., 2012. An introduction to the application of X-ray microtomography to the three-dimensional study of igneous rocks, *Lithos,* **148,** 262–276.

Bauer, D., Youssef, S., Fleury, M., Bekri, S., Rosenberg, E. & Vizika, O., 2012. Improving the estimations of petrophysical transport behavior of carbonate rocks using a dual pore network approach combined with computed microtomography, *Transp. Porous Media,* **94**(2), 505–524.

Benson, P.M., Meredith, P.G. & Schubnel, A., 2006. Role of void space geometry in permeability evolution in crustal rocks at elevated pressure, *J. geophys. Res.,* **111**(B12), doi:10.1029/2006JB004309.

Bernabé, Y., Mok, U. & Evans, B., 2006. A note on the oscillating flow method for measuring rock permeability, *Int. J. Rock Mech. Mining Sci.,* **43**(2), 311–316.

Bernabé, Y., Bruderer-Weng, C. & Maineult, A., 2003. Permeability fluctuations in heterogeneous networks with different dimensionality and topology, *J. geophys. Res.,* **108**(B7).

Black, D.K. & Lee, K.L., 1973. Saturating samples by back pressure, *J. Terramechanics*.

De Boever, E., Varloteaux, C., Nader, F.H., Foubert, A., Békri, S., Youssef, S. & Rosenberg, E., 2012. Quantification and prediction of the 3D pore network evolution in carbonate reservoir rocks, *Oil Gas Sci. Technol.–Revue d'IFP Energies Nouv.,* **67**(1), 161–178.

Brace, W.F., Walsh, J.B. & Frangos, W.T., 1968. Permeability of granite under high pressure, *J. geophys. Res.,* **73**(6), 2225–2236.

Casteleyn, L., Robion, P., David, C., Collin, P.-Y., Menéndez, B., Fernandes, N. & Rigollet, C., 2011. An integrated study of the petrophysical properties of carbonate rocks from the "Oolithe Blanche" formation in the Paris Basin, *Tectonophysics,* **503**(1–2), 18–33.

Coates, G.R., Peveraro, R.C.A., Hardwick, A. & Roberts, D., 1991. The magnetic resonance imaging log characterized by comparison with petrophysical properties and laboratory core data, in *SPE Annual Technical Conference and Exhibition,* Society of Petroleum Engineers.

David, C., 1993. Geometry of flow paths for fluid transport in rocks, *J. geophys. Res.,* **98**(B7), 12267–12278.

David, C., Gueguen, Y. & Pampoukis, G., 1990. Effective medium theory and network theory applied to the transport properties of rock, *J. geophys. Res.,* **95**(B5), 6993.

David, C. & Wassermann, J., & The_KG2B_Team, 2017. The KG^{2}B Project: a world-wide benchmark of low permeability measurement, In *Poromechanics VI,* Vandamme, M. Dangla, P. Pereira, J. M. & Ghabezloo, S., eds. American Society of Civil Engineers, Reston, VA, pp. 1153–1161.

David, C., Wong, T.-F., Zhu, W. & Zhang, J., 1994. Laboratory measurement of compaction-induced permeability change in porous rocks: implications for the generation and maintenance of pore pressure excess in the crust, *Pure appl. Geophys.,* **143**(1–3), 425–456.

Dillinger, A. & Esteban, L., 2014. Experimental evaluation of reservoir quality in Mesozoic formations of the Perth Basin (Western Australia) by using a laboratory low field nuclear magnetic resonance, *Mar. Petrol. Geol.,* **57,** 455–469.

Egger, P., 1989. Study of excavation induced rock damage at the grimsel udergrund rock laboratory, *Nucl. Eng. Des.,* **116**(1), 11–19.

Fredrich, J.T. & Wong, T., 1986. Micromechanics of thermally induced cracking in three crustal rocks, *J. geophys. Res.,* **91**(B12), 12743–12764.

Gao, Z. & Hu, Q., 2013. Estimating permeability using median pore-throat radius obtained from mercury intrusion porosimetry, *J. geophys. Eng.,* **10**(2), 025014.

Garboczi, E.J., Snyder, K.A., Douglas, J.F. & Thorpe, M.F., 1995. Geometrical percolation threshold of overlapping ellipsoids, *Phys. Rev. E,* **52**(1), 819–828.

Godel, B., 2013. High-resolution X-Ray computed tomography and its application to ore deposits: from data acquisition to quantitative three-dimensional measurements with case studies from Ni-Cu-PGE deposits, *Econ. Geol.,* **108**(8), 2005–2019.

Gueguen, Y. & Dienes, J., 1989. Transport properties of rocks from statistics and percolation, *Math. Geol.,* **21**(1), 1–13.

Gueguen, Y. & Palciauskas, V., 1994. *Introduction to the Physics of Rocks*. Princeton University Press.

Hadley, K., 1976. Comparison of calculated and observed crack densities and seismic velocities in westerly granite, *J. geophys. Res.,* **81**(20), 3484–3494.

Holzer, L., Indutnyi, F., Gasser, P., Munch, B. & Wegmann, M., 2004. Three-dimensional analysis of porous BaTiO3 ceramics using FIB nanotomography, *J. Microsc.,* **216**(1), 84–95.

Hu, Q., Ewing, R.P. & Dultz, S., 2012. Low pore connectivity in natural rock, *J. Contam, Hydrol.,* **133,** 76–83.

Hu, Q., Ewing, R.P. & Rowe, H.D., 2015. Low nanopore connectivity limits gas production in Barnett formation, *J. geophys. Res.,* **120**(12), 8073–8087.

Jiang, M., Klaver, J., Schmatz, J. & Urai, J.L., 2015. Nanoscale porosity analysis in geological materials, in *Proceedings of 14th ICSIA Acta Stereologica,* Liege, Belgium.

Josh, M., Esteban, L., Delle Piane, C., Sarout, J., Dewhurst, D.N. & Clennell, M.B., 2012. Laboratory characterisation of shale properties, *J. Petrol. Sci. Eng.,* **88–89,** 107–124.

Katz, A.J. & Thompson, A.H., 1986. Quantitative prediction of permeability in porous rock, *Phys. Rev. B,* **34**(11), 8179–8181.

Klaver, J., Desbois, G., Urai, J.L. & Littke, R., 2012. BIB-SEM study of the pore space morphology in early mature Posidonia Shale from the Hils area, Germany, *Int. J. Coal Geol.,* **103,** 12–25.

Klaver, J., Hemes, S., Houben, M., Desbois, G., Radi, Z. & Urai, J.L., 2015. The connectivity of pore space in mudstones: insights from high-pressure Wood's metal injection, BIB-SEM imaging, and mercury intrusion porosimetry, *Geofluids,* **15**(4), 577–591.

Kozeny, J., 1927. Uber kapillare Leitung der wasser in boden, *Sitzungs Ber. Akad. Wiss. Wien,* **136,** 271–306.

Mckernan, R., Mecklenburgh, J., Rutter, E. & Taylor, K.G., 2017. Microstructural controls on the pressure-dependent permeability of Whitby mudstone, in *Geomechanical and Petrophysical Properties of Mudrocks,* Rutter, E. Mecklenburgh, J. & Taylor, K., eds. Geological Society of London Special Publication, p. 454.

Monfared, M., Delage, P., Sulem, J., Mohajerani, M., Tang, A.M. & De Laure, E., 2011. A new hollow cylinder triaxial cell to study the behavior of geo-materials with low permeability, *Int. J. Rock Mech. Mining Sci.,* **48**(4), 637–649.

Paterson, M.S., 1983. The equivalent channel model for permeability and resistivity in fluid-saturated rock—a re-appraisal, *Mech. Mater.,* **2**(4), 345–352.

Rutter, E.H. & Mecklenburgh, J., 2018. Influence of normal and shear stress on the hydraulic transmissivity of thin cracks in a tight quartz sandstone, a granite, and a shale, *J. geophys. Res.,* **123**(2), 1262–1285.

Sarout, J., 2012. Impact of pore space topology on permeability, cut-off frequencies and validity of wave propagation theories, *Geophys. J. Int.,* **189**(1), 481–492.

Sarout, J., Cazes, E., Delle Piane, C., Arena, A. & Esteban, L., 2017. Stress-dependent permeability and wave dispersion in tight cracked rocks: Experimental validation of simple effective medium models, *J. geophys. Res.,* **122**(8), 6180–6201.

Scherer, G.W., Valenza, J.J. & Simmons, G., 2007. New methods to measure liquid permeability in porous materials, *Cement Concr. Res.,* **37**(3), 386–397.

Schild, M., Siegesmund, S., Vollbrecht, A. & Mazurek, M., 2001. Characterization of granite matrix porosity and pore-space geometry by in situ and laboratory methods, *Geophys. J. Int.,* **146**(1), 111–125.

Schmatz, J., Urai, J.L., Bublat, M. & Berlage, T., 2010. PetroScan—virtual microscopy, in *Geophysical Research Abstracts,* p. EGU 2010–10061.

Schull, C.G., 1948. The determination of pore size distribution from gas adsorption data, *J. Am, Chem. Soc.,* **70**(4), 1405–1410.

Smith, P.A., Alexander, W.R., Kickmaier, W., Ota, K., Frieg, B. & McKinley, I.G., 2001. Development and testing of radionuclide transport models for fractured rock: examples from the Nagra/JNC radionuclide migration programme in the grimsel test site, Switzerland, *J. Contam. Hydrol.,* **47**(2–4), 335–348.

Song, I. & Renner, J., 2007. Analysis of oscillatory fluid flow through rock samples, *Geophys. J. Int.,* **170**(1), 195–204.
Song, Y., Davy, C.A., Nguyen Kim, T., Troadec, D., Hauss, G., Jeannin, L. & Adler, P.M., 2016. Two-scale analysis of a tight gas sandstone, *Phys. Rev. E,* **94**(4), 043316.
Song, Y., Davy, C.A., Troadec, D., Blanchenet, A.-M., Skoczylas, F., Talandier, J. & Robinet, J.C., 2015. Multi-scale pore structure of COx claystone: Towards the prediction of fluid transport, *Mar. Petrol. Geol.,* **65,** 63–82.
Walsh, J.B., 1965. The effect of cracks on the uniaxial elastic compression of rocks, *J. geophys. Res.,* **70**(2), 399–411.
Walsh, J.B. & Brace, W.F., 1984. The effect of pressure on porosity and the transport properties of rock, *J. geophys. Res.,* **89**(B11), 9425.
Wang, H.L., Xu, W.Y., Cai, M. & Zuo, J., 2016. An experimental study on the slippage effect of gas flow in a compact rock, *Transp. Porous Media,* **112**(1), 117–137.
Washburn, E.W., 1921. Note on a method of determining the distribution of pore sizes in a porous material, *Proc. Natl. Acad. Sci. USA,* **7**(4), 115–116.
Wild, K.M., Amann, F., Martin, C.D., Wassermann, J., David, C. & Baria, M., 2015. Dilatancy of clay shales and its impact on pore pressure evolution and effective stress for different triaxial stress paths, in *49th US Rock Mechanics /Geomechanics Symposium 2015,* Vol. **4,** San Francisco, USA, 7, ARMA paper 15-0496, June 28th-July 1st.
Wong, T.-F., 1982. Micromechanics of faulting in westerly granite, *Int. J. Rock Mech. Mining Sci. Geomech. Abst.,* **19**(2), 49–64.
Zimmermann, G., Burkhardt, H. & Engelhard, L., 2005. Scale dependence of hydraulic and structural parameters in fractured rock, from borehole data (KTB and HSDP), *Geol. Soc. Lond. Spec. Publ.,* **240**(1), 37–45.
Zinszner, B. & Pellerin, F., 2007. A Geoscientist's Guide to Petrophysics. *Editions Technip,* IFP Publications., Paris, p. 384.

APPENDIX A: THE COMPLETE LIST OF CO-AUTHORS

[3]**The KG^2B Team:** the benchmark involved 24 rock physics laboratories around the world. The name, e-mail addresses and institution of each participant and co-author are given in Table A1.

Table A1. The KG^2B Team, list of participants and co-authors.

Participants (alphabetic order)	E-mail	Institution
Alexandra AMANN HILDENBRAND/Bernhard KROOSS/Reinhard FINK	alexandra.amann@emr.rwth-aachen.de	EMR group, Aachen University, Germany
Guillaume BERTHE/Marc FLEURY	guillaume.berthe@ifpen.fr	Institut Français du Pétrole énergies nouvelles, Rueil-Malmaison ,, France
Joël BILLIOTTE	joel.billiotte@mines-paristech.fr	MINES ParisTech, France
Christian DAVID/Jérôme WASSERMANN	christian.david@u-cergy.fr	Université de Cergy-Pontoise, France
Catherine DAVY	catherine.davy@ec-lille.fr	Ecole Centrale de Lille, France
Pierre DELAGE/Philipp BRAUN	delage@cermes.enpc.fr	Ecole des Ponts ParisTech, France
Jérôme FORTIN	fortin@geologie.ens.fr	Ecole Normale Supérieure de Paris, France
David GRÉGOIRE∗/Laurent PERRIER	david.gregoire@univ-pau.fr	Univ Pau & Pays Adour, France ∗Institut Universitaire de France
Qinhong (Max) HU	maxhu@uta.edu	University of Texas, Arlington, USA
Eberhard JAHNS	jahns@gesteinslabor.de	Gesteinslabor, Heiligenstadt, Germany
Jop KLAVER	jop.klaver@emr.rwth-aachen.de	Aachen University, Germany
Didier LASSEUX/Yves JANNOT/Alain SOMMIER	didier.lasseux@u-bordeaux.fr	I2M TREFLE, Bordeaux, France
Roland LENORMAND	roland.lenormand@cydarex.fr	Cydarex, Rueil-Malmaison, France
David LOCKNER	dlockner@usgs.gov	USGS Menlo Park, USA
Laurent LOUIS/Gregory BOITNOTT	llouis@ner.com	New England Research, White River Junction, USA
Claudio MADONNA/Florian AMANN∗	claudio.madonna@erdw.ethz.ch	ETH Zurich, Switzerland, ∗now at RWTH Aachen, Germany
Philip MEREDITH/John BROWNING/Tom MITCHELL	p.meredith@ucl.ac.uk	UCL Earth Sciences, UK
Franck NONO/Didier LOGGIA	didier.loggia@gm.univ-montp2.fr	Université Montpellier II, France
Peter POLITO	peter.Polito@jsg.utexas.edu	The University of Texas at Austin, USA
Thierry REUSCHLÉ	thierry.reuschle@unistra.fr	EOST Strasbourg, France
Ernie RUTTER	ernie.rutter@manchester.ac.uk	Univ. Manchester, UK
Joël SAROUT/Lionel ESTEBAN	joel.sarout@csiro.au	CSIRO, Perth, Australia
Patrick SELVADURAI	patrick.selvadurai@mcgill.ca	McGill University, Canada
Tiziana VANORIO/Anthony CLARK	tvanorio@stanford.edu	Stanford University, USA